Methods and Adaptations required to Perform Small-Animal MRI Scanning using a Large Bore Clinical MRI

Muhammad G. Saleh

Department of Human Biology

University of Cape Town

Thesis presented for the degree of

Master of Science

February 2012

DECLARATION

I, ……, hereby declare that the work on which this dissertation is based is my original work (except where acknowledgements indicate otherwise) and that neither the whole work nor any part of it has been, is being, or is to be submitted for another degree in this or any other university. I empower the university to reproduce for the purpose of research either the whole or any portion of the contents in any manner whatsoever.

Signature: …… ……

Date:…….

ABSTRACT

Small-animal imaging has been widely implemented to study succession of disease, therapeutic treatments and the effects of environmental insults. The gold standard non-invasive technique for following progression of heart failure in small-animal models is magnetic resonance imaging (MRI).

The aim of this project was to adapt a clinical MRI system to perform small-animal cardiac MRI. The first part of the thesis describes the adaptations required, which included design and construction of a small-animal radiofrequency (RF) coil, physical support (cradle), a core body temperature regulation system, and optimization of pulse sequences. The system was validated using a phantom and *in-vivo* in 5 healthy rats. The signal-to-noise ratio (SNR) in the phantom was 91% higher using the small-animal coil compared to the standard head coil. SNRs of 7 ± 2 and 18.9 ± 0.6 were achieved in myocardium and blood, respectively, in healthy rats and MR left ventricular mass (LVM) was highly correlated with (r=0.87) with post-mortem mass.

In the second part of the study, left ventricular remodeling (LVR) was investigated in a non-reperfused model of myocardial infarction (MI) in 5 sham and 7 infarcted rats. Rats were scanned at 2 and 4 weeks post surgery to allow for global and regional functional and structural analyses of the heart. Images were of sufficient quality to enable semi-automatic segmentation using Segment.

Significant increase in end-systolic volume (ESV) was observed in MI rats at 2 weeks post surgery. At 4 weeks post surgery, end-diastolic volume (EDV) and ESV of MI rats were significantly higher than in sham rats. Ejection fraction (EF) of MI rats dropped significantly at 2 weeks and a further significant drop was observed at 4 weeks indicating contractile dysfunction. Wall thickness (WTh) analyses in MI rats at 4 weeks revealed significant reduction in end-diastolic (ED) wall thickness in the anterior region due to necrosis of myocytes. In the posterior region, WTh was significantly higher due to LV hypertrophy. At end-systole (ES), the MI rats revealed significant decrease in WTh in the anterior and lateral regions. MI rats suffered reduction in systolic wall thickening in all regions of the heart, indicating global contractile dysfunction.

Jesus was once asked, "Who taught you ethics?"He replied, "No one. I saw the ugliness of ignorance and strayed away from it."

Introduction to Islam

Islamic Humanitarian Service

Amirul Momineen Ali ibn Abi Talib (peace be upon him) said: 'O believer, knowledge and manners are values of yourself, thus make efforts in gaining knowledge, as much as your knowledge and manners increase, your status and value would also increase, because through knowledge you would be guided to your Lord and through manners you would be able to serve the Lord in the best way and one who has good manners would become eligible for the guardianship and proximity of God. Hence, accept good advice, so that you may be saved from the punishment of God."

Introduction to Islam

Ayatollah Ibrahim Amini

To my beloved parents, sisters, teachers, relatives,
and friends.

Table of Contents

List of Figures

List of Tables

Acknowledgements

Drs. Ernesta Meintjes, Neil Davies and Thomas Franz supervised the work. They provided the context, expert ideas, advice, support and numerous resources required for the implementation of this work. Alkathafi Alhamud, Dr. Andre J.W. van der Kouwe, Dr. Lawrence Wald and Azma Mareyam – from the Martinos Center for Biomedical Imaging at Massachusetts General Hospital – for the guidance on designing and building the small-animal coil. Dr. Bruce Spottiswoode provided ideas on pulse sequence optimization. Sarah-Kate Sharp performed surgeries on rats. Dr. Vijay Dahya provided advice and guidance on image segmentation. Fulufhelo Masithulela provided assistance with the transport and handling of the animals. Charles Harris constructed the rat bed; Mogammad Fakier constructed the temperature regulation system. Radiographers Nailah Maroof and Marie-Louise de Villiers for advice on data collection.

The following organizations have provided the resources used in this work: University of Cape Town and Cape Universities Brain Imaging Centre.

Funding was provided by the South African Research Chairs Initiative of the Department of Science and Technology and National Research Foundation of South Africa, the Medical Research Council of South Africa, and NIH grant R21AA017410.

Funding through the following scholarships: South African Research Chairs Initiative MSc scholarship, and the University of Cape Town international student scholarship.

1. Introduction

Small-animal imaging, both in vitro (fixed specimen) and in-vivo (living animals) has become an increasingly important facet of medical research in fields such as pharmacology, toxicology and biomedical. The ability to obtain information on the anatomical or functional changes in organs of small animals has lead to a better understanding of succession of disease, therapeutic treatments and the effects of environmental insults [1]. In addition, the ability to perform repeated non-invasive imaging on the same animal provides us with the opportunity to study progression of disease. In most of the literature the term "Small-animal Imaging" is often used interchangeably with "MR microscopy", although they operate with different image resolutions, as will be discussed later.

Magnetic Resonance Imaging (MRI) is a medical imaging method used for visualizing the internal structure of the human body. It is one of the major tools of radiology that can be applied to every part of the human body. It has also been adapted for use with small animals due to its rich contrast capable of displaying soft tissues such as brain, heart, and muscles. Other common modalities such as Computed Tomography (CT) do not provide the soft tissue contrast or have the versatility of MRI [2]. In addition, CT requires high radiation dose to achieve high signal-to-noise ratio (SNR) and adequate resolution for the small size of rodent organs [2]. The dose can be harmful to the animal and result in interference with longitudinal studies.

The extension of clinical MRI to small-animal MR imaging requires increased resolution in all dimensions which results in decreased signal strength. To overcome this, strong magnets, small-animal radiofrequency (RF) coils, optimized image acquisition sequences, and physiological and physical support for animals are required. Additional challenges include controlling biological motion and gross body motion in order to prevent any artifacts or blurring in the image. Finally, the cost to purchase and maintain an MR system is far greater than for other imaging modalities.

Despite the aforementioned challenges, the valuable information obtained from small-animal MR imaging makes it well worth the investment. It is inherently digital and can be 3 dimensional (3D), so that one can interactively view images along any axis to understand the complex structure of the animal [3]. Unlike other modalities, it provides better soft tissue

contrast and spatial resolution. The ability to perform non-invasive imaging on the same animal over a prolonged period of time reduces the number of animals needed. The latter benefit adheres with one of the principles (Reduction) of humane experimental techniques.

1.1 Description of the Problem

Small-animal models are used extensively in the development of treatments for heart failures that result from myocardial infarctions (heart attacks). The Cardiovascular Research Unit (CVRU) has a well established rat heart failure model. The techniques currently used for determining functional parameters of the heart are echocardiography and catheter based haemodynamic measurements. The latter, though powerful, is an end point method and animals must be killed after measurements are taken, and the former, though non-invasive, is relatively imprecise as it relies mostly on geometric assumptions that work well only in normal hearts [4]. The gold standard non-invasive technique for following heart failure development over time in small-animal models is magnetic resonance imaging. This technique allows for precise measurements of the heart whilst it beats and thus gives accurate data on its functional status.

This project aims to establish a low cost small-animal magnetic resonance imaging (MRI) facility at the Cape University Brain Imaging Centre (CUBIC) situated at Tygerberg Hospital for in-vivo cardiac imaging of small-animal models (e.g. rat, mouse) of myocardial infarction.

1.2 Objectives

The objectives of the study were to:

1. Investigate the requirements to adapt a human MRI for small-animal scanning;
2. Implement the changes required in 1) above at CUBIC;
3. Set up and optimize a cardiac MRI sequence to perform small-animal cardiac MRI at CUBIC;
4. Perform cardiac MRI scanning of 5 pilot (healthy) rats to test the small-animal MRI system and sequence;
5. Scan 12 rats, 7 with an induced myocardial infarction and 5 with thoracotomy, at 14 and 28 days post-operatively to assess functional and structural impairment;
6. Correlate MRI findings with histology.

1.3 Thesis Outline

The thesis has two major parts: Part I: MRM setup and Part II: Application of MRM to study animal model of LVR in non-reperfused MI.

Part I includes the following chapters:

In Chapter 2 I present a basic introduction to MRI, followed by ways to address the challenges of small-animal MRI. Later on, requirements for extending clinical MRI to small-animal MRI are described.

Chapter 3 describes the design and construction of an RF birdcage coil and physical support for the animal. It also describes the optimization of the pulse sequence and gating system, as well as SNR and CNR measurements of a phantom and cardiac images from healthy animals.

Chapter 4 describes the results of the initial MRM setup, including SNR and CNR measurements.

In Chapter 5 the results presented in chapter 4 are discussed. This chapter marks the end of Part I

Part II includes the following chapters:

Chapter 6 provides background on rodent models of myocardial ischemic disease and methods for performing image analyses.

Chapter 7 describes the methodology used for performing animal surgery, preparation for cardiac MRM, imaging parameters, and the methods implemented for image analyses.

Chapter 8 describes results of image analyses in all rats. Results include structural and functional analyses in sham and infarcted rats.

Chapter 9 provides a discussion of the results presented in chapter 8, the performance of the pulse sequence, and the segmentation software that was used to analyze the cardiac images.

Chapter 10 presents the overall conclusions drawn from the study as well as recommendations for future work.

This work has been submitted to a peer reviewed journal, and it is under review, also part of this work appears in conference proceedings, as shown below:

- Saleh MG, Sharp S-K, Alhamud A, Spottiswoode BS, van der Kouwe AJW, Davies NH, Franz T, Meintjes EM. Long-term Left Ventricular Remodelling in Rat Model of Non-reperfused Myocardial Infarction: Sequential MR Imaging using a 3T Clinical Scanner. Journal of Biomedicine and Biotechnology, 2012, In review
- Sirry MS, Davies NH, Kadner K, Saleh MG, Spottiswoode BS, Meintjes EM, Masithulela F, Zilla P, Franz T. Geometrical Modeling of Myocardial Biomaterial Injectate in a Rat Heart Utilizing Magnetic Resonance Imaging and Histology, in 8th South African Conference on Computational and Applied Mechanics (SACAM). 3rd-5th September 2012: Johannesburg, South Africa. In review.
- Masithulela F, Davies NH, Sharp S-K, Saleh MG, Spottiswoode BS, Meintjes EM, Zilla P, Franz T. Rat Heart Ventricle 3D Geometrical Reconstruction - Towards Understanding of Cardiac Mechanics in Myocardial Infarction. ICMIB 2012 - International Conference on Medical Information and Bioengineering, Mar 24-25, 2012, Shenzhen, China.
- Masithulela F, Davies NH, Sharp S-K, Saleh MG, Spottiswoode BS, Meintjes EM, Zilla P, Franz T. Rat Heart Left and Right Ventricle 3D Geometrical Reconstruction and Validation using 3T Magnetic Resonance Imaging. CHPC National Meeting 2011: Better HPC and Data-curation Adoption, Better Research and Industrial Development, Dec 7-9, 2011, Pretoria, South Africa.
- Sirry MS, Davies NH, Kadner K, Saleh MG, Spottiswoode BS, Meintjes EM, Masithulela F, Zilla P, Reddy BD, Franz T. Combined 3D Geometrical Reconstruction of a Rat Heart and Myocardial Biomaterial Injectate from Magnetic Resonance Imaging and Histology. CHPC National Meeting 2011: Better HPC and Data-curation Adoption, Better Research and Industrial Development, Dec 7-9, 2011, Pretoria, South Africa.

Part I: MRM Setup

2. Background and Literature Review

2.1 From Small-Animal MRI to Magnetic Resonance Microscopy

The progress of clinical MRI to small-animal imaging involves increasing resolution to tens and hundreds of microns resulting in decreased SNR [1]. However, improvements in hardware and techniques since 1980 have resulted in greater SNR. As the SNR is improved, microscopic spatial resolutions can be achieved [5]. MR images with in-plane resolution and slice thickness ranging from 49 to 390 μm and 200 to 1500 μm, respectively, such as is the case in small-animal imaging, are widely termed MR microscopy images [4,6]. Thus, the term "MR microscopy" (MRM) will be used instead of small-animal imaging in the remainder of the thesis.

2.2 Basic Principles of Magnetic Resonance Imaging

The MR signal originates from the protons in the nucleus of the atoms of the object being scanned. The protons spin about their own axes and create a magnetic field, called a magnetic dipole moment (mdm). When the mass number (ie. protons + neutrons) is odd, a net magnetic field exists. The common nuclei detected using MRI are Hydrogen (^{1}H), Fluorine (^{19}F), Sodium (^{23}Na) and Phosphorus (^{31}P). Hydrogen is the most commonly imaged nucleus due to its high natural abundance and high abundance in tissue. The hydrogen nucleus comprises one proton only.

A powerful external magnetic field (B_o) exerts a torque on the mdm created by the spinning proton in the hydrogen nucleus. The torque causes the mdm's to precess about B_o (Figure 2.1). The frequency at which the mdm's precess around the external magnetic field is given by the Larmor equation,

$$\omega = \gamma B_o \tag{2.1}$$

where ω is the angular precession or Larmor frequency and γ is the gyromagnetic ratio. Slightly more of the protons line up parallel to B_o than anti-parallel to it, resulting in a net magnetization (M_o) parallel to B_o.

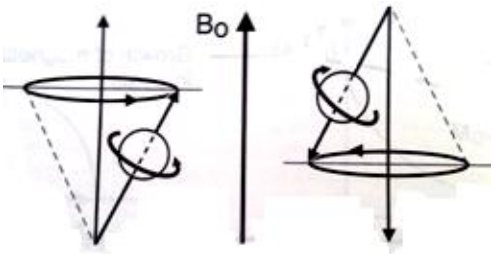

Figure 2.1: Two protons, one aligned against the field and another with the field [7].

This magnetization cannot be detected by a receiving coil because it is not an oscillating signal. A radiofrequency (RF) pulse (electromagnetic wave) applied briefly with a frequency equal to the Larmor precession frequency (resonance) flips the magnetization, resulting in components both parallel (called longitudinal magnetization M_z) and perpendicular (called transverse magnetization M_{xy}) to the main magnetic field. After termination of the RF pulse, the M_{xy} component precesses about the main magnetic field at the Larmor precession frequency, which induces a voltage in an RF coil. This is the MR signal.

M_{xy} dephases due to interactions between individual spins (internal inhomogeneities) and external magnetic field inhomogeneity. The rate at which M_{xy} decays is called the transverse relaxation time (T2) and is given by

$$M_{xy}(t) = M_o e^{-t/T2} \tag{2.2}$$

At the same time, but due to a different and independent process, M_z grows back to its equilibrium value. This process is called spin-lattice or longitudinal relaxation time (T1) and is given by

$$M_z(t) = M_o(1 - e^{-t/T1}) \tag{2.3}$$

T2 decays 5 to 10 times faster than T1 recovery. These constants depend primarily on the kind of tissue being imaged. T1 increases with increasing magnetic field. With the application of multiple RF pulses and magnetic field gradients in three orthogonal directions that are applied at different times in a sequence, one can achieve enough spatial information to create an image. The time interval between successive RF pulses is called the repetition time (TR). The time between the RF pulse and the signal acquisition is termed time to echo (TE). Unlike T1 and T2 which are inherent properties of tissues (hence fixed), TR and TE can be controlled

and adjusted by the operator to enhance image contrast. Table 2.1 shows T1 and T2 values of fat, cerebrospinal fluid (CSF) and gray matter (GM) at 1.5 T.

Table 2.1: Representative values of T1 and T2 of different human body tissues at 1.5T [8].

Tissue	T1 (ms)	T2 (ms)
Fat	250	60
Gray matter (GM)	950	100
Cerebrospinal fluid (CSF)	4500	2200

Figure 2.2 demonstrates the concept of T1 weighting. If a 90 degree RF pulse is applied every 500ms, the longitudinal magnetization in CSF and Gray matter will not recover completely prior to subsequent RF pulses. As such, the transverse magnetization following the RF pulse will be less for these tissues, resulting in lower signal compared to fat, keeping in mind that it is only the transverse component of the magnetization that gives rise to signal.

Figure 2.3 demonstrates the concept of T2 weighting by appending a T2 decay curve on the T1 recovery curve after an RF pulse. At TE1, fat will be brighter while at TE2 CSF will be brighter, due to the fact that the transverse magnetization of fat dephases more rapidly. Signals measured at short TR and TE create T1 weighted images while signals measured at long TR and TE create T2 weighted images. The computer programme that controls the timing and shape of the pulses, switching of the gradients, digitization of signals, image reconstruction and image display is called a pulse sequence [1].

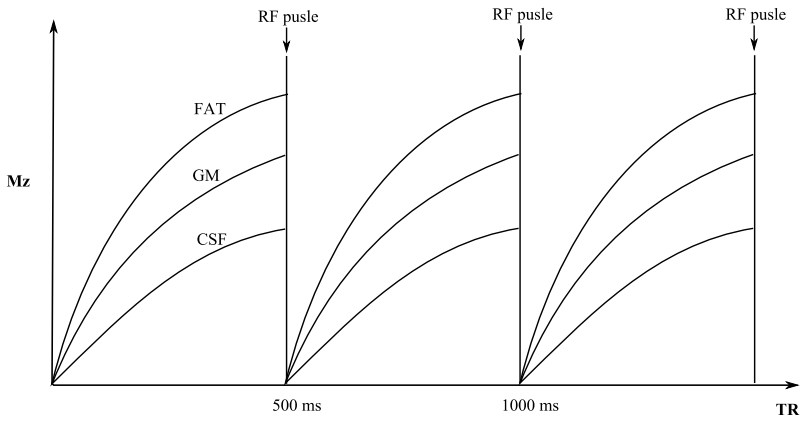

Figure 2.2: T1 recovery curve of fat, GM and CSF. 90^{o} pulses applied every 500ms. TR: repetition time; Mz: longitudinal magnetization.

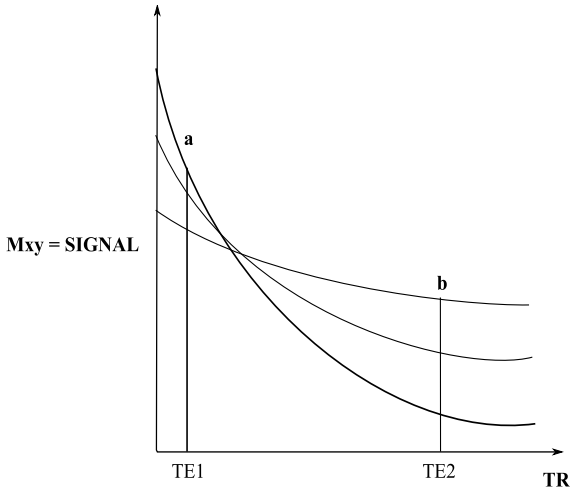

Figure 2.3: T2 decay curve appended to the T1 recovery curve after an RF pulse. TR: repetition time; TEx: echo time; Mxy: transverse magnetization

2.3 Challenges of MRM

The preceding introduction to MRI outlined challenges of small-animal MRI. One of the most vital elements of any imaging modality is signal-to-noise ratio (SNR). It is clear that signal diminishes as the pixel volume (voxel) decreases. Equation 2.4 gives the relationship between SNR and voxel volume.

$$SNR \propto \frac{voxel\ volume\sqrt{N_{acq}N_yN_z}}{\sqrt{BW}} \tag{2.4}$$

in which N_{acq} is acquisition time, BW is the receiver bandwidth and N_y is phase encoding steps and N_z is slice encoding steps.

Figure 2.4 demonstrates clearly the difference in pixel size between a human brain image and that of a mouse. Typical voxel volumes for human scanning are of the order of 5 mm^3, as compared to 0.000064 mm^3 in the case of a mouse or rat brain. Since the signal is produced by small volumes of tissue, this leads to a substantial reduction in SNR [9]. One way to increase SNR is by increasing the magnetic field strength (B_o), which increases magnetization and the resulting signal in the receiving coil. However, noise levels increase linearly with Larmor frequency. High magnetic fields also lead to greater chemical shift artifacts, increased tissue heating, and are expensive to install and maintain [10]. Optimizing RF coil design and increasing total data acquisition time (N_{acq}) provide the most significant improvements in SNR. SNR increases as the square root of the imaging time (Equation 2.5), if the noise is

uncorrelated from one measurement to another [8]. Longer acquisition time (prolonged experiments) is, however, an expensive and impractical way of increasing SNR, as it introduces risks associated with extended periods of anesthesia.

$$SNR = \sqrt{N_{acq}}\ \frac{s(k)}{\sigma_m(k)} \tag{2.5}$$

where $\sigma_m(k)$ is the standard deviation of noise and s(k) is the signal.

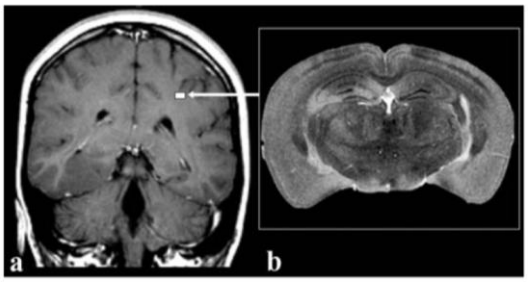

Figure 2.4: a) Clinical MR image of human brain imaged at 1x1 mm^2 in-plane resolution and 5mm slice thickness b) mouse brain imaged at 40x40 µm^2 with a 40 µm slice thickness. White arrow (square) shows the size of mouse brain relative to human brain. Voxel volumes of the human brain must be reduced by about 80000 to visualize mouse brain at the same anatomic level as human brain [11].

2.4 Radiofrequency Coils

The radiofrequency (RF) coil is the most crucial component of MRI, which is used for signal excitation and reception. Reducing the dimensions of the RF coil from human size to rodent size can result in a significant gain in SNR while still covering the anatomical region of interest (ROI) [12]. The common coils implemented in MRM include surface coils and birdcage coils [13].

Surface coils, such as carotid artery or wrist coils, enhance SNR and provide better spatial resolution when visualizing the ROI adjacent to the coil [14]. Alternatively, phased array coils, an array of small surface coils (Figure 2.5) decoupled from each other, are used to cover a large field of view (e.g. mouse spine) with optimum SNR as long as the ROI is very close to the body surface [15].

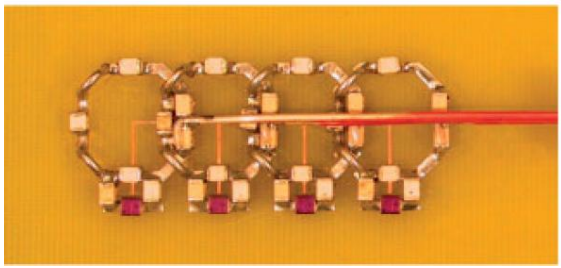

Figure 2.5: Top view of the mouse spine array. The four elements are coupled capacitively; the connecting cables all run into a common virtual ground plane [15].

The birdcage coil, which is often both a transmit and receive (T/R) coil (Figure 2.6), is the most widely used coil for whole body in-vivo imaging of rats and mice because of its ability to achieve high B_1 field homogeneity [13,16]. This results in increased SNR, according to the equation:

$$SNR \propto V_s B_1 \omega^2 \tag{2.6}$$

where V_s is the sample volume, and B_1 is the magnetic field associated with the radiofrequency pulse. The major advantage of this coil is that at greater depths, the birdcage coil provides better signal-to-noise ratio compared to phased array coils [13].

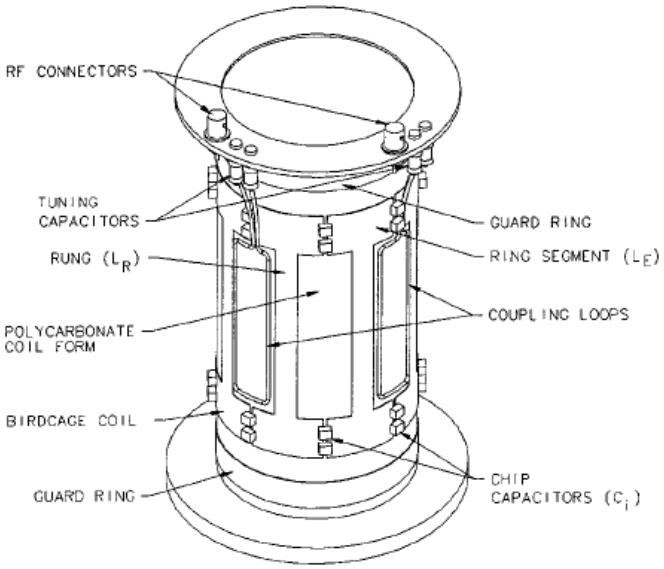

Figure 2.6: Typical Birdcage coil [16].

2.4.1 Tuning Circuit

An RF coil must be matched to the electronic devices through a tuning (resonant) circuit. A typical tuning circuit is shown in Figure 2.7. It is made up of capacitors for storing electrical energy in the electric field between their plates; and inductors for storing energy in the magnetic field induced by coil winding.

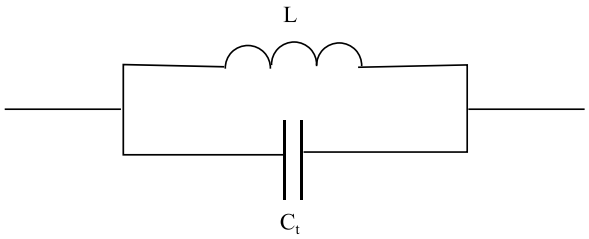

Figure 2.7: Typical tuning circuit design. L: Inductor; C_t: Tuning capacitor.

When a fully charged capacitor is connected to an inductor, charge starts to flow to the inductor, creating magnetic field around it, and hence a change in flux. Eventually, all the charge in the capacitor will be discharged through the inductor. However, according to Lenz's law, the induced electromagnetic force (emf) induced opposes change in flux, which will cause the capacitor to retain the charge. This cycle (in the absence of internal resistance) continues forever at the resonance frequency of the circuit, described as $1/2\pi\sqrt{LC_t}$. In reality the coil has an internal resistance (R), and thus the resulting impedance of the circuit is then given by:

$$Z = \frac{R^{2+}\,\omega^2 L^2}{R - i\omega L[1 - \frac{R^2 C_t}{L} - \omega^2 L C_t]} \tag{2.7}$$

The resonance condition applies when the imaginary part of the equation is equated to zero, as show below:

$$1 - \frac{R^2 C_t}{L} - \omega^2 L C_t = 0 \tag{2.8}$$

Therefore, for a particular value of capacitor, C_t (tuning capacitor), and inductor L, the resonance frequency can be determined using the Equation 2.8. For most coils R << ωL, and quality factor (Q), defined as ωL/R, the impedance of the circuit at resonance ($Z_{resonance}$) is then $Q\omega L$. Q is the measure of efficiency of the tuning circuit.

2.4.2 Matching circuit

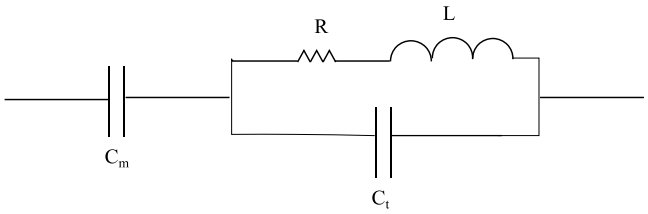

Figure 2.8: Matching capacitor (C_m) connected to tuning circuit design. L: Inductor; C_t: Tuning capacitor; C_m: Matching capacitor; R: Internal Resistor.

In order to transfer maximum power available from a power source to the load, the load impedance (Z_L) must be equal to the complex conjugate of the source impedance (Z_S), as shown below:

$$Z_L = Z_S^* \tag{2.9}$$

where * indicates complex conjugate sign. Since, generally, neither the load nor the source impedance can be changed, a matching network is established. As shown in Figure 2.8, a matching capacitor, $C_{m,}$ is connected in series with the typical tuning circuit to match the load to input impedance of 50 Ω. The input impedance (Equation 2.10) is now given by the following equation (assuming R << ωL, as before):

$$Z = \frac{R}{(1-\omega^2 L C_t)^2} + \frac{i[1-\omega^2 L(C_m+C_t)]}{\omega C_m(1-\omega^2 L C_t)} \tag{2.10}$$

which yields for resonance and matching conditions

$$\omega^2 L(C_m + C_t) = 1 \text{ and } \frac{R}{\omega^4 L^2 C_m^2} = 50\Omega \tag{2.11}$$

respectively. The constraints (Equation 2.11) determine the values of tuning and matching capacitors for a particular coil and resonant frequency. In our study, the RF coil was tuned at the resonant frequency of 123.25 MHz for a 3T scanner.

2.4.3 Quadrature detection

One important aspect in the birdcage RF coil is to generate circularly polarized magnetic field. This is done by the help of a quadrature hybrid circuit. When a sinusoidal current is applied to the quadrature circuit, it splits into two currents of equal amplitude and frequency (Figure 2.9), but one will experience a phase shift of 0^o (in-phase) while the other 90^o (out of

phase), resulting in a circularly polarized magnetic field. A 40% enhancement in SNR is achieved for a circularly polarized system relative to a linear polarized system from the same coil, as well as a factor of 2 reduction in specific absorption rate [13].

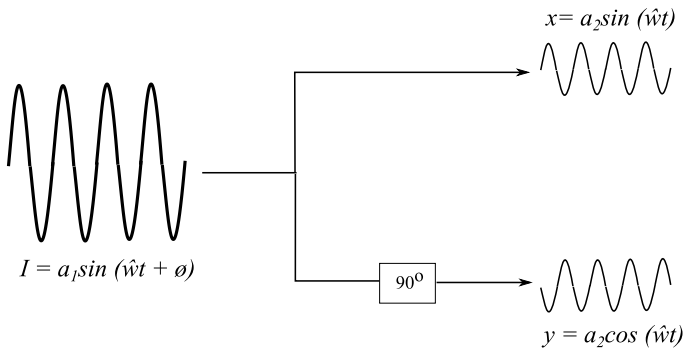

Figure 2.9: Quadrature hybrid circuit used for generation of two currents (*x* and *y*) with a relative phase shift of 90^{o}. The resulting currents produce a circularly polarized magnetic field.

2.5 MRI Hardware

In general, MRM is performed on high field scanners (≥ 4.7T) with high gradients strength, faster slew rates, and a small bore specifically designed for rodents [17-20]. However, these scanners are expensive and not available at many institutions. Nevertheless, small-animal imaging has been performed successfully in standard clinical MRI scanners with dedicated RF coils, which improve signal reception [12,21-22]. In order to achieve high resolution images without substantial image degradation due to cardiac motion, the MR must be equipped with high gradient strengths and faster slew rates [12]. For example, a 3T TIM Trio MR scanner (Siemens, Erlangen, Germany) is equipped with gradients and slew rates that are capable of acquiring cardiac images in small animals with in-plane resolution of about ~200 µm [23]. Alternatively, specialized gradient inserts with custom RF coils can be developed to achieve maximum gradient strengths and faster slew rates [24].

2.6 Cardiac MRM

2.6.1 Challenges

The most difficult organ to image is the heart due to motion resulting from both the cardiac contraction and respiration. The rate at which the rodent heart beats is high compared with the human heart rate. The average heart rate for mice is about 300 to 800 beats per minute and 300 to 400 beats per minute for rats, compared to roughly 60 beats per minute for humans

[25]. The artifacts are further exacerbated by the anatomy of the rodent heart. The size of the rat heart is about 18 mm while that of the mouse is about 8 mm [26-27]. An additional challenge is respiratory motion at a rate of about 50 to 60 breaths per minute. Hence, a technique to compensate for cardiac and respiratory motion is vital for successful cardiac MRM.

2.6.2 Physiological Monitoring and Gating

Electrocardiogram (ECG) gating is a requirement for cardiac MRI in humans and animals. It is the most established gating technique in MRM [28]. It employs the R-wave from ECG to capture images of the heart at different time points within a cardiac cycle. The resultant image is a frozen image of the heart. Pediatric or adult electrodes can be utilized to acquire ECG signals from animals. The ECG signal is, however, degraded by RF pulses and gradient switching during imaging [12]. Clinical scanners also often cannot detect rat and mouse heart rates as they are well above the human heart rates, as previously explained. Besides cardiac motion, respiratory motion also induces artifacts in the images. Thus, rodent specific equipment is necessary to minimize artifacts for successful data acquisition.

Rodent specific cardiac monitoring and gating equipment is available and sold by different vendors, such as the Model 1025 System (SA Instruments, Inc, USA). Such systems are stand-alone systems developed to cope with fast heart beats, smaller ECG signals as well as electrical interference generated by rapid gradient switching, and can communicate with a standard PC. Furthermore, these systems can monitor ECG signals from rodents as well as use them to trigger a clinical scanner at specific time points specified by the user [26,29].

Aforementioned systems also include a respiratory gating system, allowing acquisition of data either during the expiration or inspiration period of the breathing cycle. In the absence of respiratory gating, signal averaging works well in reducing respiratory artifacts [26,29].

Although gating reduces artifacts, it is important to define and optimize gating parameters to suit the physiology of the animal. Optimization can lead to significant increases in signal intensity and reduction in noise levels. Cassidy et al. [30] implemented user-defined cardiac and respiratory gating parameters that matched very well with mouse physiology, and it resulted in 285% increase in signal intensity and 575% decrease in total noise intensity when compared with other gating strategies, as illustrated in Figure 2.10.

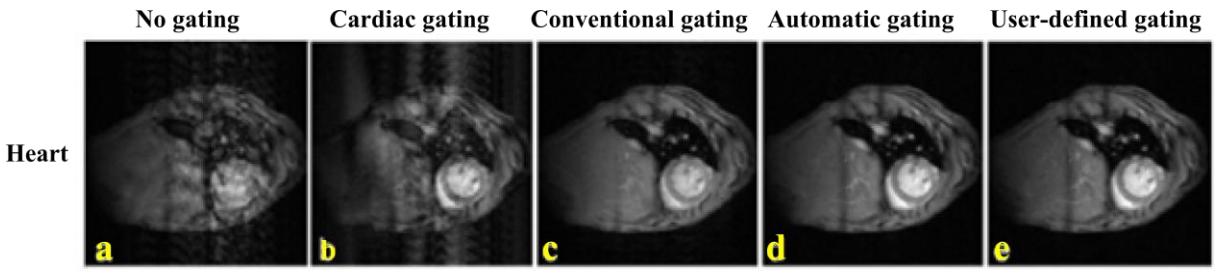

Figure 2.10: Images acquired using a gradient echo sequence with different gating methods (a-e). e: shows short-axis images of the heart with myocardium delineated very well with the lowest level of noise compared with other gating methods [30].

2.6.3 Pulse Sequence

In clinical MRI, almost all functional cardiac imaging are performed using segmented gradient echo (GE) sequences and, more recently, balanced steady state free precession (bSSFP) sequences. However, images from the bSSFP sequence suffer from banding artifacts that are related to how short repetition time (TR) can be made and the homogeneity of the magnetic field [31]. Thus, spoiled GE is the most common sequence implemented in cardiac MRM for structural and functional assessment of rat hearts [27-28,32-35].

Different MRI vendors have different names for the spoiled GE sequence, and some of them are spoiled Fast Low Angle Shot (FLASH), a spoiled gradient echo (SPGR). It comprises of series of excitation pulses which are each separated by a repetition time (TR) and data is acquired after the application of the excitation pulse at a specific time, called echo time (TE), as shown in Figure 2.11. Slice selective gradient (G_{SS}) is used concurrently with RF pulses to form a slice selection lobe. The amplitude of G_{SS} and bandwidth of RF pulse determine the slice thickness. Phase encoding gradient (G_{PE}) and frequency encoding gradient (G_{FE}) are used to spatially encode NMR signals with unique phase and frequency, respectively, to each spin isochromat at a distinct spatial location along the gradient direction.

The term *spoiled* means that the residual transverse magnetization that remains at the end of TR is manipulated so that it does not contribute signal in subsequent TR [36]. Spoiling can be achieved either by means of gradient pulses (gradient spoiling) or RF pulses (RF spoiling). RF spoiling is the most preferred and powerful technique for removing residual magnetization. The basic idea is to increment the RF phase angle quadratically which causes the resulting transverse magnetization (M_{xy}) to have a phase angle that is offset relative to the

residual magnetization that persists from prior magnetization. This way new signal from most recent RF pulse will dominate while residual magnetization will phase cancel [37].

In cardiac MRM spoiled GE sequence has been frequently used to scan rodents heart for functional and structural assessment [26-27]. Also it has been implemented in non-clinical scanners for measuring infarct size [38-39]. Through this sequence contrast generated between myocardium and LV blood depends on T1 weighting of the tissue and inflow effect of the blood [40].

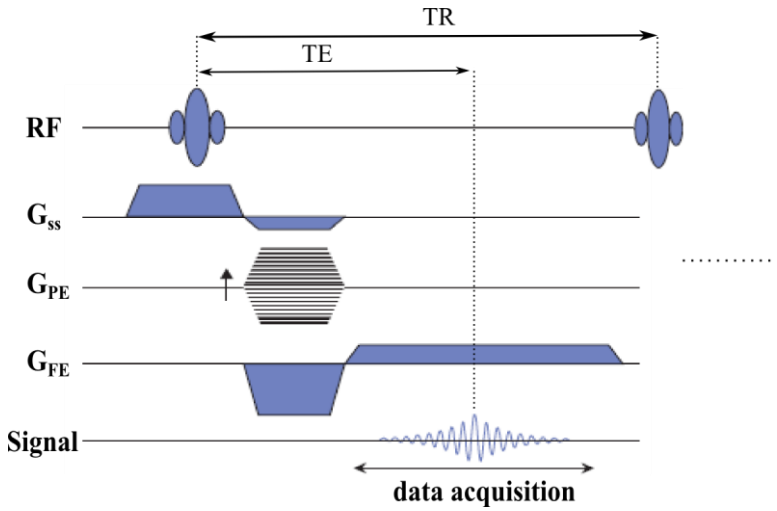

Figure 2.11: The basic elements of the gradient echo MR imaging sequence. Amplitude is shown vertically, time horizontally. RF: radiofrequency pulse; G_{SS}: slice selective gradient; G_{PE}: phase encoding gradient; G_{FE}: frequency encoding gradient; TR: repetition time; TE: echo time.

This sequence is capable of achieving short TR and TE values, making it compatible with fast heart beats (between 300 and 600 bpm). The parameters typically used in ECG triggered GE sequences are echo time (TE) of the order of 2-5 ms, TR of the order 4-11 ms, and flip angle between 25^{o} and 45^{o} [32-34]. These parameters may vary and are limited by MRI hardware specifications. This sequence can use either prospective or retrospective triggering. Prospective ECG gated segmented GE sequence is triggered subsequent to R-wave peak detection and allows images to be captured with high overall SNR and improves the contrast to noise ratio (CNR) between blood and myocardial wall compared to retrospective triggering [41].

2.6.4 Cine Imaging and Scan time

GE sequence can be gated by external signals, such as cardiac and respiration signals from a rat, and can perform fast oblique imaging using the principles of *k-space* segmentation (cine imaging) for data acquisition [42-43].

The basic design for cine imaging is shown in Figure 2.12. After the R-wave trigger, 1 line of k-space is acquired for every cardiac frame. This process is repeated as many times as necessary, requiring multiple heart beats to acquire all the lines of k-space in order to compose the multiple frames of a cine image stack, thus creating a movie (cine) of the beating heart [19,40]. The number of heartbeats per slice acquisition is equal to the number of phase encoding steps (N_y). The imaging planes most widely used are two and four chamber long-axis views, and a short-axis view as shown in Figure 2.13.

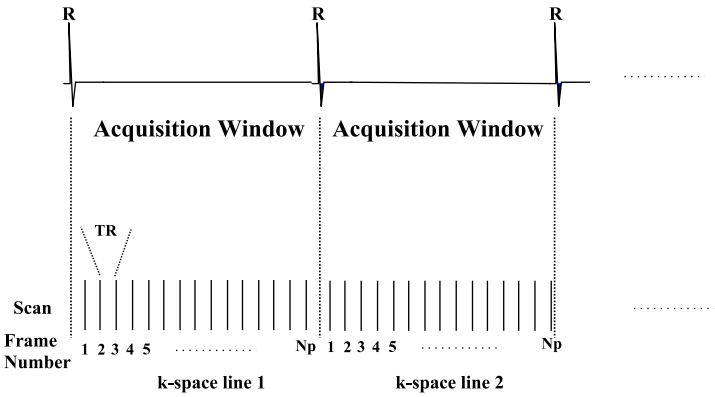

Figure 2.12: Prospectively ECG-triggered cine FLASH sequence. Only 1 k-space line is acquired per cardiac frame per cardiac cycle. This cycle continues until all lines (phase encoding steps) have been acquired. TR: repetition time; N_y: number of phase encoding steps.

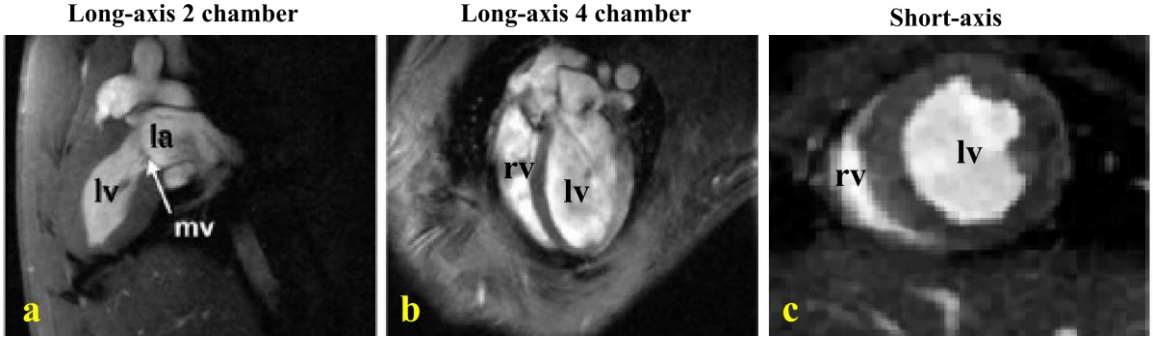

Figure 2.13: Standard orientations: a) 2 chamber long-axis view; b) 4 chamber long-axis view and, c) short-axis view. mv: mitral valve, la: left atrium, lv: left ventricle, rv: right ventricle [19].

Scan time depends on various imaging and gating parameters. In ECG-gated pulse sequence, scan time depends on following parameters: number of phase encoding steps (N_y), number of lines of k-space per cardiac frame per cardiac cycle (segment, (S)), average R-R time and number of signal averaging (N_{acq}). It can be calculated as:

$$Scan\ time = N_y * N_{acq} * RR/S \tag{2.12}$$

2.7 Setup for MRM

It is important to maintain the animal in one position and immobilize it during MR scanning to obtain images with high resolution. Any body movement not only produces a blurred image but also introduces artifacts due to spatial encoding errors, cause interference with the anatomical details of the subject, and result in inaccurate observation [1]. In order to immobilize the animal it is important to anesthetize them. With longer image acquisition, anesthetics tend to interfere with the normal body function, such as metabolic rate, and cause body temperature to drop causing death. The cold temperature of the lab and in the bore of the MRI can also cause body temperature to drop. Heating elements such as heat lamps, microwavable heat pads, or hot water flowing through a tube around the subject's body can induce heat and raise the temperature of the body. It is important to maintain physiological temperatures as overheating can harm the animal by causing burns [44]. Thus, animal preparation for MR imaging is vital to prevent the problems mentioned above. The preparation includes physical support, administration of anesthetics, body temperature monitoring and control, and physiological monitoring (Figure 2.14).

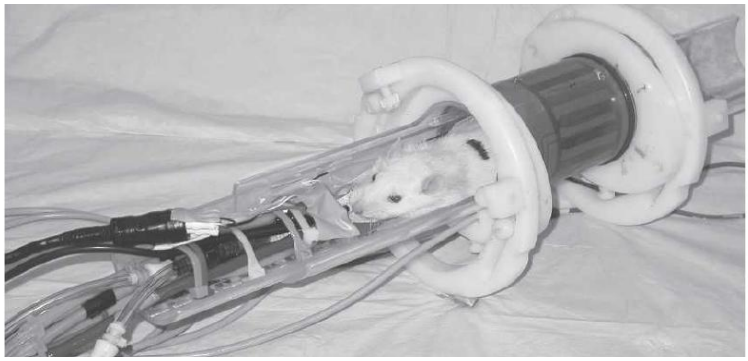

Figure 2.14: A 250 g rat prepared for imaging in a 2T system using a 6 cm diameter birdcage coil. The animal is lying on a Plexiglas cradle and is anesthetized with isoflurane delivered by mechanical ventilation. The hoses to the left are for ventilation gases and the black cables carry signals from ECG electrodes on the foot pads, airway pressure transducer on the breathing valve attached to the

endotracheal tube, and body temperature from a thermistor in the rectum. The lower cable connects the coil to the MR scanner [1].

2.7.1 Physical Support

Physical support for the animal is important so that it can be transferred from one place to another without harm or changing its position [12]. The device must provide the physical support and fit in the MRI coil [44]. It acts as a bed for the animal. Since the shape of the animal body is nominally cylindrical, the shape of the device must have a semi-circular cross-section. It must easily slide in and out of the RF coil [1]. The type of material used should not be metallic or ferromagnetic as these materials tend to cause interference with MRI images and can be dangerous when attracted to the magnet [7,45]. Another important aspect to take into consideration is the size and weight of the animal. The device must be large and strong enough to support the size and weight, and provide correct alignment of the animal in order to obtain the best possible images.

2.7.2 Anesthetics

It is important to restrain animals to prevent any gross body motion, such as crawling out of the magnet. Anesthetics are used to immobilize animals in order to prevent any gross body motion during scanning, also to prevent artifacts and achieve high resolution images [44]. Anesthetics can be administered through inhalation or by injection [46]. Inhalation has a faster effect than injection as it delivers the agent to the central nervous system by pulmonary circulation, and it allows remote adjustments of anesthetic length, depth, as well as rapid recovery [1,47], thus preventing any harm to the animals. Some studies [48-50] anesthetized their animals by air flow through the animal's nose while another [51] anesthetized with a single dose of intraperitoneal injection. Other common routes of administration are subcutaneous, intramuscular and intravenous [47].

There are different types of anesthetics available [47]. The common ones used on animals during MR scanning are ketamine/xylazine (K/X) and isoflurane [17,51-53]. Previous studies [54-55] have shown that K/X causes bradycardia (reduced heart rate), decreases cardiac output and increases breathing rate significantly compared to isoflurane. Although isoflurane preserves cardiac function, it should be maintained as low as possible for a stable sleep as it causes significant reduction in breathing rate.

Although anesthetics ensure restraint, it causes the core body temperature of the animal to drop [44]. Thus, it is important to have a controlled exogenous heat supply to maintain core body temperature at normal levels.

2.7.3 Core Body Temperature Monitoring and Control

Rodents' core body temperature drop rapidly due to their large surface area to body mass ratio and rapid metabolism [56]. In addition, as mentioned earlier, anesthetics have the undesirable effect of interfering with the core body temperature of the animal, causing the animal to rapidly lose body temperature, especially in the cold bore of the magnet. Hence, it is essential to have an exogenous heat supply to maintain the core body temperature of the animal in order to perform long experiments. Although temperature drop can induce hypothermia, overheating can significantly harm the animal and cause burns. There are several methods to radiate heat to the animal including heating pads placed beneath the animal, heat lamps directed towards the body, or hot water and air flow through a tube around the animal's body. Hot water was the preferred method implemented by [48,57] as water has high thermal conductivity (0.58 W m^{-1} K^{-1}) compared with air (0.024W m^{-1} K^{-1}). Therefore, water can transfer large amounts of heat through a unit thickness of material compared to air.

Body temperature can be monitored using a rectal temperature sensor. Temperature sensors are mainly composed of metal parts but some probes are made of fiberoptics. Fiberoptic probes are necessary in the MRI environment as it will not induce any artifacts [58]. Any change in temperature can be regulated by altering the temperature of the heating element.

2.8 Summary

The major challenge to extending clinical MRI to MRM is the attainable SNR. This challenge can be solved by implementing a dedicated small-animal RF coil, large enough to cover the anatomical ROI. Optimizing the pulse sequence is another requirement to achieve high resolution images.

GE sequences are widely used for scanning human and rodent hearts. Prospective triggering of this sequence results in acquisition of data with high SNR and CNR between myocardium and blood. Cardiac and respiratory gating is necessary to reduce artifacts caused by cardiac and respiratory motion.

MRM requires physical support for the comfort and proper alignment of the animal. In addition, anesthetics is a major requirement to immobilize the animal and prevent artifacts in images. Since anesthetics interferes with the animal's core body temperature, and the cold magnetic bore of the MRI further exacerbates this condition, a heating element is required to raise the core body temperature of the animal. Temperature control is necessary to maintain the temperature of the heating element to prevent harm to the animal.

3. MRM Design and Setup

3.1 Design and Construction of RF coil

One of the major hurdles in MRM is the attainable SNR. The most reasonable and efficient way of acquiring images with high SNR is by reducing the dimensions of RF coil, small enough to cover the anatomical ROI [16]. For this reason, a custom made transmit-receive (T/R) small-animal birdcage RF coil was used in this study (Figure 3.1). The coil was built in collaboration with Massachusetts General Hospital (MGH).

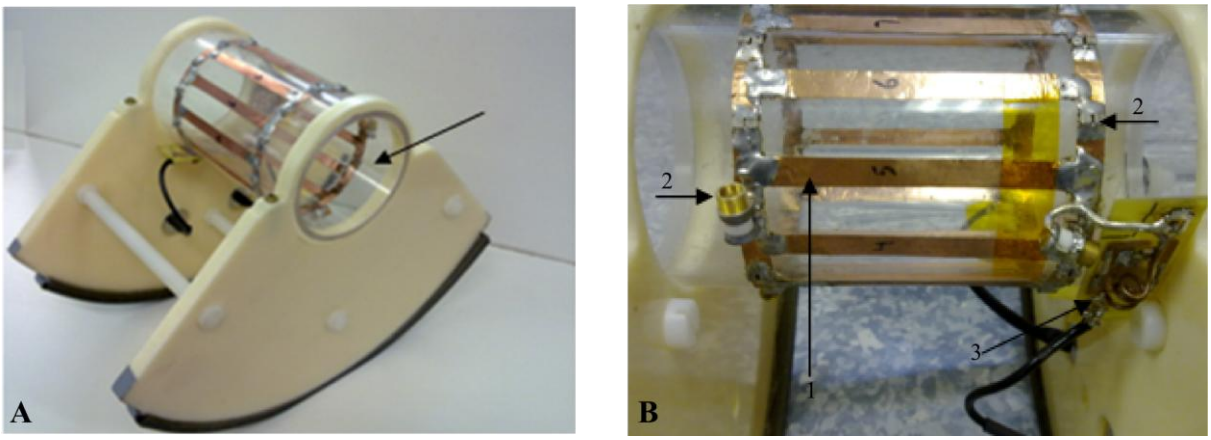

Figure 3.1: Circularly polarized, T/R and 70 mm internal diameter volume birdcage RF coil. A) The space (arrow), where the rat will be placed for imaging. B) The coil has several electrical components, such as copper foil (arrow 1), capacitors (arrow 2) and trap circuit (arrow 3).

One important factor that affects SNR directly in a birdcage coil is magnetic filling factor (η_F) [13]. The η_F depends not only on the volume of the sample (V_S), but also on the volume of the coil (V_C) and is given by

$$SNR \propto \eta_F$$

$$\eta_F \approx \frac{V_s}{V_c} \tag{3.1}$$

Hence, a decrease in the volume of the coil results in an increase in the η_F, and consequently a substantial gain in SNR. Before construction, it was important to consider the dimensions of the animal to be studied in order to maximize the filling factor of the RF coil and obtain images with optimal SNR. In agreement with previous studies [47,59], rats can grow from a

body weight of 210 g to approximately 370 g over the 4-week period typically used to study post myocardial infarct left ventricular remodeling (LVR). The dimensions of a 370 g rat were measured and are summarized in Table 3.1. Table 3.2 summarizes the length and diameter of the RF coil, as well as the length of electrical components used to construct the coil.

Table 3.1: Dimensions of rat.

Animal	Rat
Weight	370 g
Diameter of chest	54 mm
Length of body w/o tail	15 cm
Heart's long-axis	1.5-1.8 cm
Heart rate (anesthetized animal)	300 bpm (average)
Field of view	50-85 mm

Table 3.2: Dimensions of the birdcage coil and values of electrical components.

Coil	Volume Birdcage Coil
Length	145 mm
Internal diameter	70 mm
Width of copper foil	7 mm
Number and length of copper foil	12 legs and 83 mm
Resonant frequency (for 3T scanner)	123.25 MHz

Figure 3.2 shows the front section of the rat birdcage coil, which includes capacitors and the trap circuit affixed around the rim of the coil. Also, it shows two cables (cable 1 and 2) extending outwards from the coil. Cable 1 transmits signal at 0° phase while cable 2 transmits at 90° phase. The signals are 90° out of phase, which results in a circularly polarized magnetic field as explained in previous chapter.

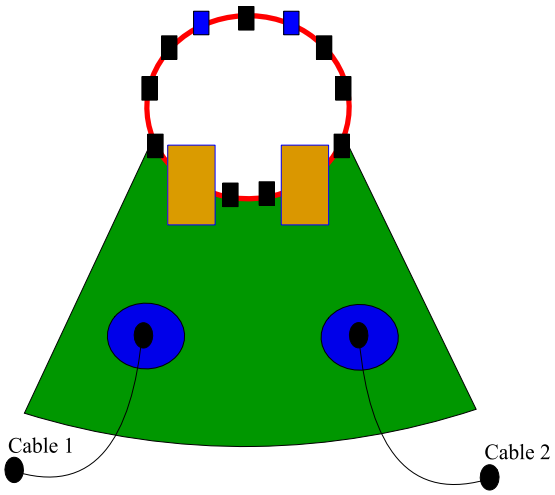

Figure 3.2: Front section of the rat birdcage coil. Several electrical components are attached to the rim (red circle), such as trap circuit (yellow rectangle), variable capacitors (blue rectangle) as well as fixed capacitors (black rectangle). Two cables (Cable 1 and 2) extending outwards for transmission and reception of signal.

The rat birdcage coil comprises of 7 mm wide copper foil rungs mounted on the external surface of a Perspex tube with an outer diameter of approximately 72 mm. The inner diameter (Figure 3.1) that the rat must fit into is 70 mm. There are 12 copper foil rungs equally spaced around the outer surface of the tube. Figure 3.3 shows the schematic diagram of RF coil and its equivalent circuit. The copper foil rungs are presented as inductors, and capacitors are arranged at both ends of the copper foil rungs.

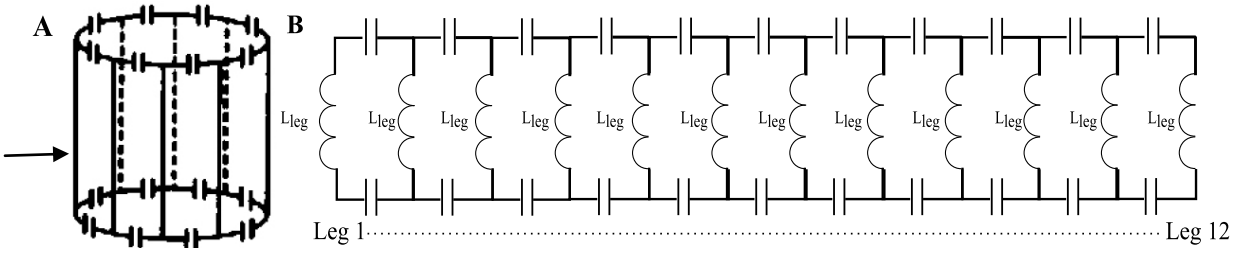

Figure 3.3: (A) Schematic diagram of the RF coil with 12 legs (arrow showing one of the legs) and B) its equivalent circuit. Capacitors attached at both ends of the legs. L_{leg}: copper foil represented as inductor

Figure 3.4 illustrates the trap circuit, the matching circuit and the tuning capacitors. Coaxial cables are connected to the MRI scanner through which signals are transmitted and received. The trap circuit, made up of inductors and capacitors, behave as high impedance at the resonant frequency, preventing any electrical or RF (noise) interference with the signal from the subject. Matching and tuning circuits are made up of fixed and variable capacitors. The

matching circuit is used to match the coil impedance to a standard impedance of 50 Ω, while the tuning circuit is used for tuning the coil to the resonant frequency of 123.25 MHz for a 3T scanner.

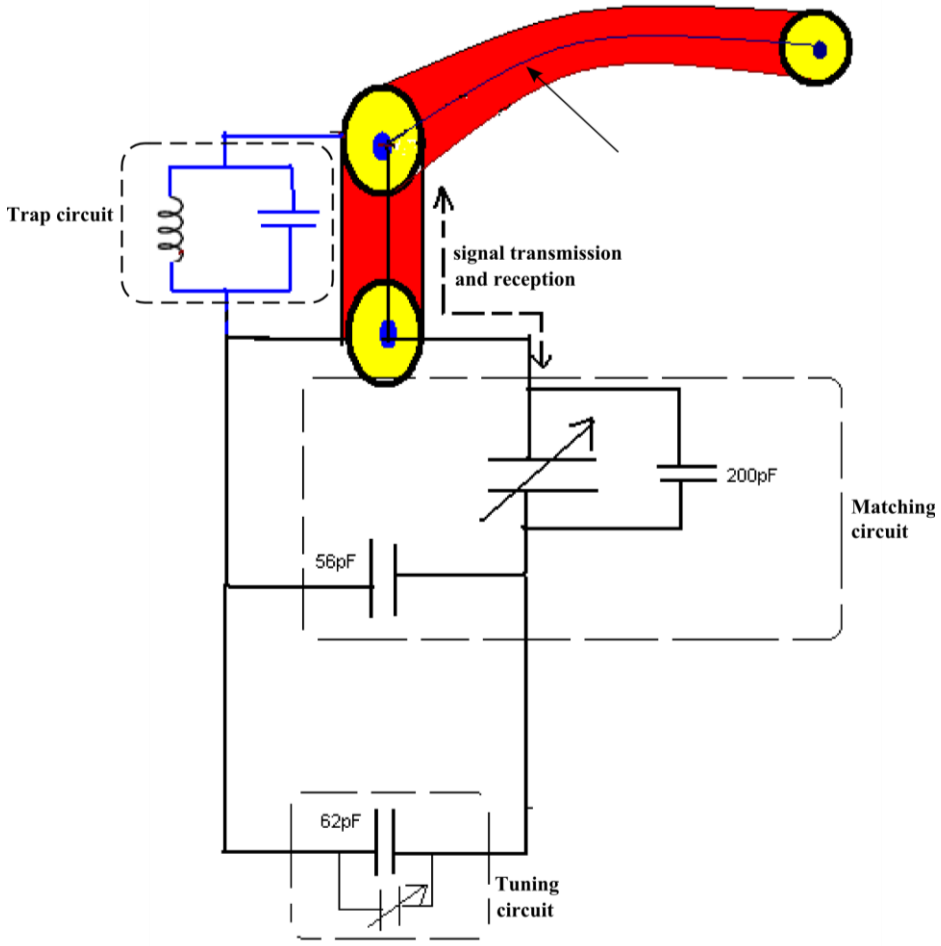

Figure 3.4: One of the feed sides to the coil, containing matching tuning and trap circuits. Coaxial cable (black arrow) responsible for transmitting and receiving signal. Matching, and tuning circuit made up of fixed and variable capacitors. Trap circuit made up of capacitors and inductors.

3.2 Construction of Physical Support

As previously explained, physical support is a vital component of the MRM system as it allows the animal to be transferred from one place to another without harm or changing its position. It should also be able to accommodate the cables for monitoring ECG and core body temperature. It should include a heating system to maintain the animal's body temperature and a channel for delivery of anesthetics. Figure 3.5 shows the rat bed (cradle) that was designed and constructed to accomplish this.

Since a rat's body as well as the shape of the RF coil is nominally cylindrical, the cradle was designed to be semi-cylindrical. The material that was employed to build the bed was a non-metallic material, called high density polyethylene (HDPE). It is compatible with a strong magnetic environment, thus ensuring safety of the animal. Furthermore, it is light, yet strong enough to support the animal's weight. It is available at low cost, is durable, can easily be obtained in any hardware shop, and can withstand frequent use in a controlled clinical environment.

Our aim was to design a cradle that can fit comfortably in the birdcage coil. It should also be appropriately sized to accommodate the animal, have a channel to allow flow and maintenance of anesthesia, and be equipped with a heating source to raise the temperature of the animal, as illustrated in Figure 3.6.

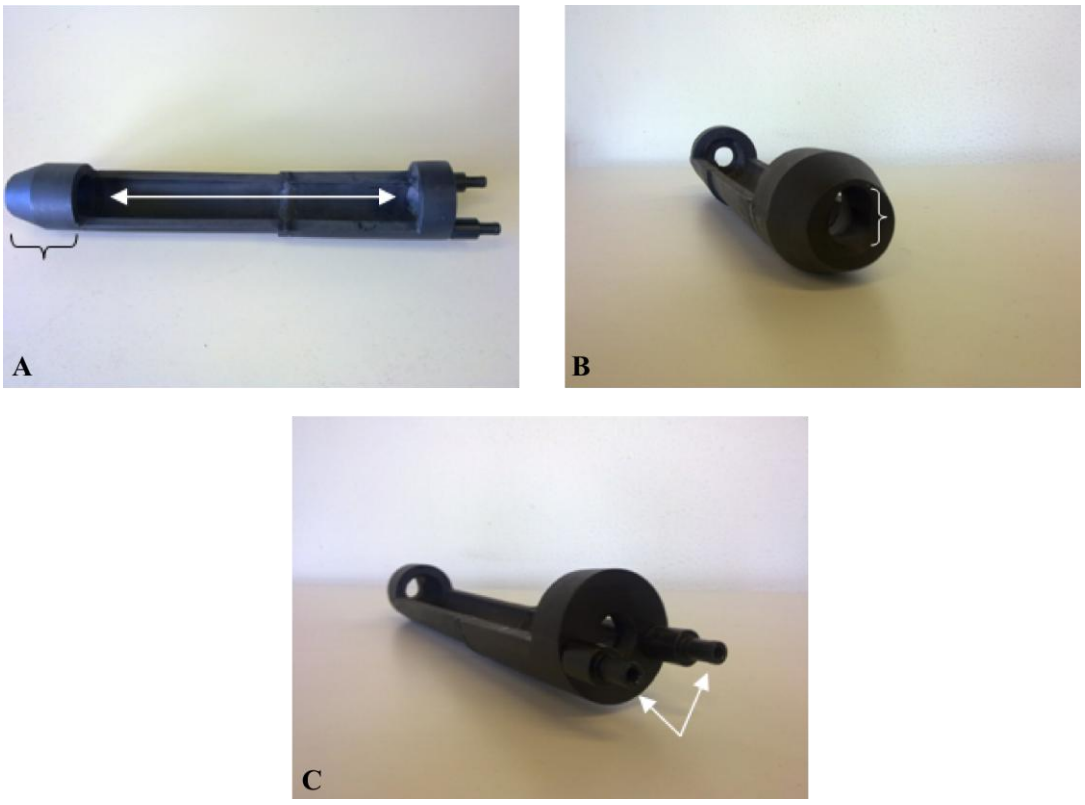

Figure 3.5: Images of the cradle at different views. A) Top view shows rat's resting area (arrow) and nose cone (curly bracket). B) Front view showing inlet for anesthetics (curly bracket). C) Inlet and outlet of hot water (arrows).

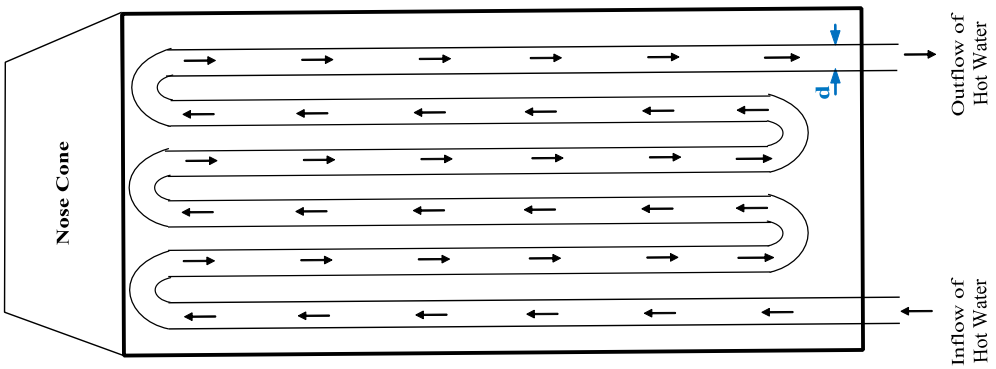

Figure 3.6: Cradle design and specifications. Top view of the cradle demonstrating the path of the water flowing in and out of the cradle. Nose cone for anesthetics delivery. d: diameter of the tube.

Since the inner diameter of the RF coil is 70 mm, the cradle (Figure 3.7) was constructed to have outer diameter (D_e) of 67 mm. This allows easy insertion and removal of the cradle from the coil.

Since the diameter of the chest of a 370 g rat was about 54 mm (Table 3.1), the internal diameter (D_i) of the cradle was chosen to be 57 mm (Figure 3.7). This size allows enough space to contain a rat as well as all the cables for monitoring ECG, respiration and temperature signals.

As previously mentioned, anesthesia is essential for immobilization during imaging. Inhalational anesthetics are preferred over injectable ones because they permit easy adjustment of the intensity of anesthesia and rapid recovery [47]. Some studies have used mechanical ventilation during imaging [60-61], which can be complicated as an MRI compatible ventilator is required. This technique also requires endotracheal intubation which has the potential to damage the respiratory tract and is not appropriate for longitudinal studies [62]. Other studies have used respiratory routes to administer anesthetics. Exposure of anesthetics through respiration involves either a mask, whole body exposure or a nose cone. Mask exposure is frequently used for large animals such as dogs. We implemented a whole body exposure technique for anesthetizing rats before commencement of imaging. To this end, we constructed an inhalation chamber that had two inputs: one for inflow of anesthesia gas and the other connected to an air filter canister (A.M. Bickford Inc. USA) to remove excess halogenated anesthetic gases from the chamber, as shown in Figure 3.8.

Nose only exposure is mainly used for rodents, and it is a more precise technique than whole body exposure [62]. Several studies have used the nose only exposure method to supply and

maintain anesthesia while imaging [48-50,63]. Our design includes a nose cone with an inlet for anesthesia flow and maintenance as shown in Figure 3.5 and Figure 3.7.

The combination of MR imaging environment, cryogenically cooled magnets, cold surroundings of the lab and depressive effects of anesthesia drop the core body temperature of the rat. Thus, exogenous heat supply is required for body temperature control. We embedded a flow system into the cradle that allows the flow of hot water through tubes in the wall of the cradle (Figure 3.9). The cradle was connected to a water tank and a pump to ensure continuous flow of water to avoid any hotspots and ensure animal safety. Due to the limited size of the cradle, the diameter (d) of the tubes was sized to 5 mm (Figure 3.6 and Figure 3.7). The tubes are arranged in three loops (Figure 3.6). These loops were extended to cover the whole cradle, allowing sufficient heat dissipation to the whole body of the animal.

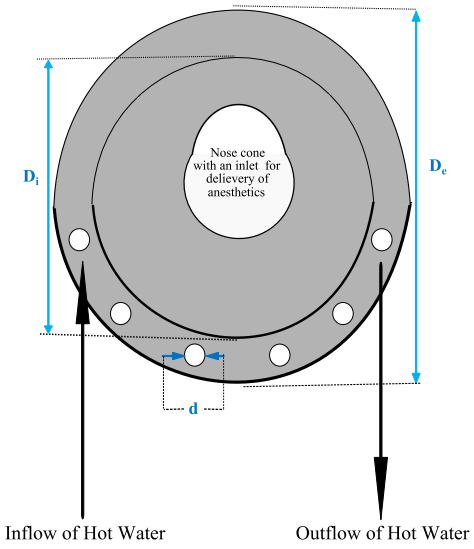

Figure 3.7: Axial view of the cradle, illustrating the inlet for anesthetics and arrangement of tubes along the bed of the cradle (arrow). d: diameter of the tube. D_e: external diameter of the cradle. D_i: internal diameter of the cradle.

Figure 3.8: Induction chamber (arrow 1) with air filter (arrow 2) interconnected via plastic tubes.

Figure 3.9: Initial stage of construction of the cradle with tubes for water flow system (arrow) embedded in the wall of the cradle.

3.3 Cardiac and Respiratory Gating System

Rat heart is the most difficult organ to scan due to cardiac motion (average 300 bpm). In addition, thoracic movement due to breathing, which occurs at a rate ranging between 60 and 120 breaths per minute, further complicates in-vivo cardiac MRM.

Cardiac and respiratory gating addresses the problem of the cardiac and respiratory motion very effectively. A small-animal monitoring and gating system (Model 1025, System SA Instruments, Inc, USA) was purchased (Figure 3.10). This system includes two modules: (a) the ECG/Temperature module measures the temperature of the animal using a small rectal fiberoptic probe, ECG using two subdermal or surface electrodes, and respiration by coupling one of the ECG leads to the animal's abdomen; (b) the Control/Gating module via optical fibers sends data to the PC for display and receives instructions from the PC to control measurement and gating functions. ECG and respiratory traces and gating were generated by the Control/Gating Module and sent to the MR system. This system was customized according to a rat's cardiac and breathing rate.

Figure 3.10: Small-Animal Monitoring and Gating system.

3.4 Testing the Gating System at CVRU

The gating system was first tested at the UCT Cardiovascular Research Unit laboratory (CVRU) using a 350 g rat. The animal was sedated in the induction chamber with an air flow containing 5% isoflurane. After that, it was placed over the Perspex bed with a nose cone supplying continuous air flow with isoflurane concentration reduced to 1.5%, as shown in Figure 3.11.

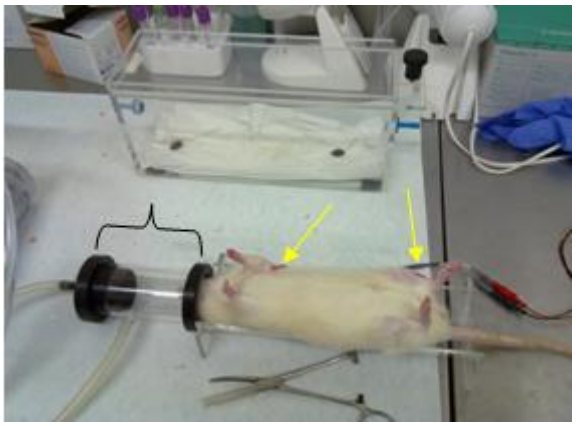

Figure 3.11: Subdermal needles attached to the front and rear limbs of the rat (arrows). Nose cone supplying continuous air flow mixed with isoflurane (curly bracket).

Subdermal electrodes were securely attached to the animal's front and rear legs for acquiring ECG signals (Figure 3.11). The rat was placed on the cradle and slid into the coil, as shown in Figure 3.12.

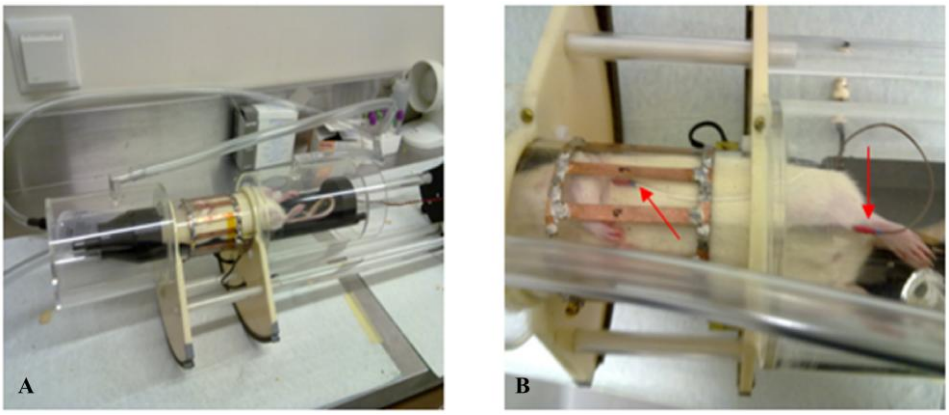

Figure 3.12: Images of the rat in the RF coil. A) Rat placed on the cradle and slid into the coil. B) A closer view of the rat in RF coil. Arrows: subdermal electrodes attached to the rat's limbs.

ECG cables were connected to the ECG/Temperature module. This module was connected to the Control module, which was transmitting data to the computer via a Universal Serial Bus (USB) cable (Figure 3.13A). Figure 3.13B, shows the ECG signals displayed on the computer using software called PC-SAM (SA Instruments, Inc, USA). Unfortunately, respiration signals were not displayed because they are magnetic field dependent.

Figure 3.13: Images of modules and a notebook displaying ECG signals. A) ECG/Temperature module (arrow 1) transferring data to Control module (arrow 2), which is responsible for transmitting data to the notebook. B) ECG signals displayed using software, called PC-SAM. No respiration signals are observed on the software as they are magnetic field dependent.

3.5 Temperature Control and Regulation

Although an exogenous heat supply is important to raise the temperature of a rat while being scanned, overheating may cause harm or even death. Any change in the rat's core body temperature should be regulated by altering the temperature of the heating element.

An MR compatible temperature heating system is available (SA Instruments, Inc, USA) for rats, but they are very expensive. For this project, we designed a temperature regulation system that was manually controlled by altering the heat level of a water heater.

The temperature regulation system comprised three main components: Water reservoir/tank, water heater and water pump. These components are also used in other environments, such as landscaping and home aquariums, and we modified these existing solutions to fit our specific design requirements.

The water tank with an inbuilt heater (manually controlled) was available at the Department of Human Biology (Figure 3.14). A pump (Figure 3.15) was purchased for R500. It was a

submersible filter pump (Dolphin P-2500) commonly used in aquariums with a maximum power rating and flow speed of 30 W and 1500 litres/hour, respectively. This pump can sustain a substantial amount of heat, and has enough power to circulate water from the tank to the cradle and vice versa. Insulated tubing was used as a conduit for water flowing from the tank to the cradle, and vice versa (Figure 3.14B).

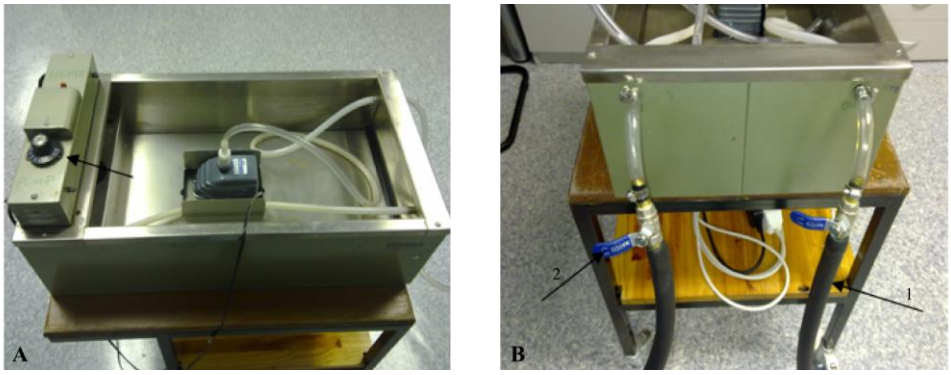

Figure 3.14: Images of the water tank, heater and a pump. A) Water tank with a manually controlled heater (arrow). B) Insulated tubing connected to the tank (arrow 1) act as conduit for water flow between the cradle and tank. Ends of insulated tubing connected to a manually controlled valve (arrow 2).

Figure 3.15: Water pump (Dolphin P-2500) used for transferring water from the tank to the cradle, and vice versa.

A temperature sensor, called Pt-100, was immersed in the tank filled with water to measure the temperature of the water. This was necessary to prevent the water from overheating as this will cause harm to the rat. The water temperature was displayed on a digital thermostat display monitor (ENDA ETC1311) as shown in Figure 3.16. The core body temperature of the rats, measured by a rectal temperature sensor, was used to determine the optimum

temperature of the water necessary to maintain the rat at 37°C. Results are explained in the following chapter.

Figure 3.16: Electronic equipment displaying temperature of water in °C. Current display shows that the temperature of water is 35 °C.

3.6 Initial MRM Set up at CUBIC

Subsequent to the construction of the cradle as well as procurement of the water tank and a pump, we assessed the system at CUBIC for any leakages or loose connections. The cradle was connected to the water tank using insulated tubing, as shown in Figure 3.14, and the pump was submerged in the tank. Manually controlled valves were connected to the end of the tubing (Figure 3.14) to prevent any water flow in the case of leakage. Initially, the set up was done outside the scanner room, and the pump along with the heater was switched on to check for any leakages or loose connections.

After the success of aforementioned test, the water tank was positioned outside the scanner room (Figure 3.17A). The tubes were fed into the scanner room through a waveguide (Figure 3.17B), and the cradle was slid into the coil and positioned on the MRI bed (Figure 3.17C). The temperature of the water was gradually increased by the heater and simultaneously pumped to the cradle through the tubes around the animal's body (Figure 3.6 and Figure 3.9). The temperature of the water was increased to 50 °C to assess the integrity of the cradle at high temperatures. Results are explained in the following chapter.

The length of the insulated tubing connecting the water tank to the cradle was 9 m. Flow of water through such an extended distance could cause the temperature of the water to fall drastically along the way, which could render the cradle ineffective in maintaining the temperature of the rat. Hence an experiment was performed to determine the difference in temperature between the cradle and the water in the tank. A thermometer was placed on the

cradle's resting area (Figure 3.5A) with its reservoir bulb firmly coupled to the cradle. Results are explained in the following chapter.

Figure 3.17: Set up at CUBIC before initiation of rat imaging. A) Water tank connected to the cradle via insulated tubing (arrow). B) Insulated tubing passing through the waveguide. C) Cradle positioned in the RF coil on the MRI bed.

We next performed a scan to determine whether the water flow causes artifact in the images. We imaged a mole rat, fixed in formalin. Initially, we implemented a FLASH sequence, but there was not enough signal as the rat was very dehydrated. We used bSSFP sequence with the following parameters: field of view (FOV) = 91×121 mm, flip angle (α) = 60°, TE = 2.96 ms, TR = 5.91 ms, matrix 256 × 192, pixel bandwidth = 590 Hz/pixel and signal averages = 1. The phase encoding direction was flipped from Anterior-Posterior to Left-Right direction. Imaging duration was about 1 second. Results are explained in the following chapter.

The water flow caused artifacts in the images. To address flow artifacts, we removed the first and last loops of the water channel in the attempts of avoiding the artifacts interfering with the ROI, as shown in Figure 3.18. In addition, we placed a soft low-resilience polyurethane (LRPu) foam pillow that conforms to the exact contours of the animal's body inside the cradle. Using the same mole rat, imaging sequence and parameters mentioned above we tested the corrected flow channel. Results are explained in the following chapter.

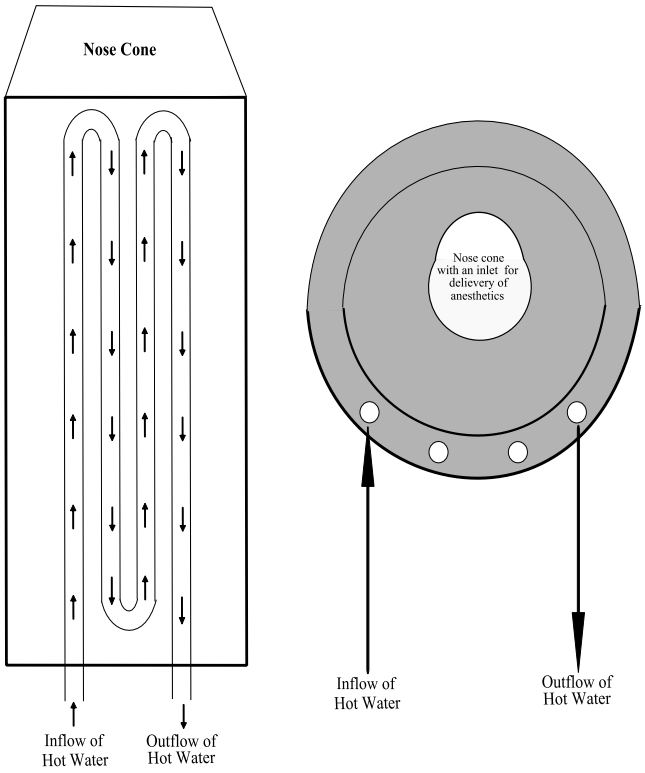

Figure 3.18: Images of the cradle with reduced number of loops.

3.7 Imaging Protocol

All scans were performed on a MAGNETOM Allegra 3T MRI scanner (Siemens, Erlangen, Germany) in Cape Town, South Africa. This brain-only system is well suited to animal scanning due to its smaller bore, maximum gradient strength of 40 $mT.m^{-1}$ and slew rate of 400 $mT\ m^{-1}\ ms^{-1}$. A custom built, circularly polarized, 70 mm (inner diameter) birdcage radiofrequency (RF) coil was used to transmit and receive the signal.

In this project a spoiled GE sequence (fast low angle shot (FLASH) sequence) was used to obtain cine cardiac images for functional and structural assessment of rat heart. The sequence achieves high in-plane isotropic resolution (~ 200 μm).The minimum number of segments attainable was 1 k-space line per cardiac frame per cardiac cycle, resulting in very high temporal resolution. Only slice thickness required changing from 1.5 mm to 1 mm, which was achieved by reducing the time bandwidth product.

In this project the sequence was cardiac and respiratory gated (double gating) to acquire cardiac cine images of rat's heart for functional and structural assessment (Figure 3.19). Cardiac images were acquired only during the end of expiration. Immediately after the

detection of R-wave, RF pulses were triggered. Due to the variation in R-R interval, acquisition window time was set such that RF pulses are applied over 70 to 85% of the cardiac cycle. The last few seconds of the R-R interval was not used because it was utilized to detect another R-wave in combination with heart rate variability. Figure 3.19 shows 1 k-space line acquired per frame per cardiac cycle, allowing images to be captured with high temporal resolution.

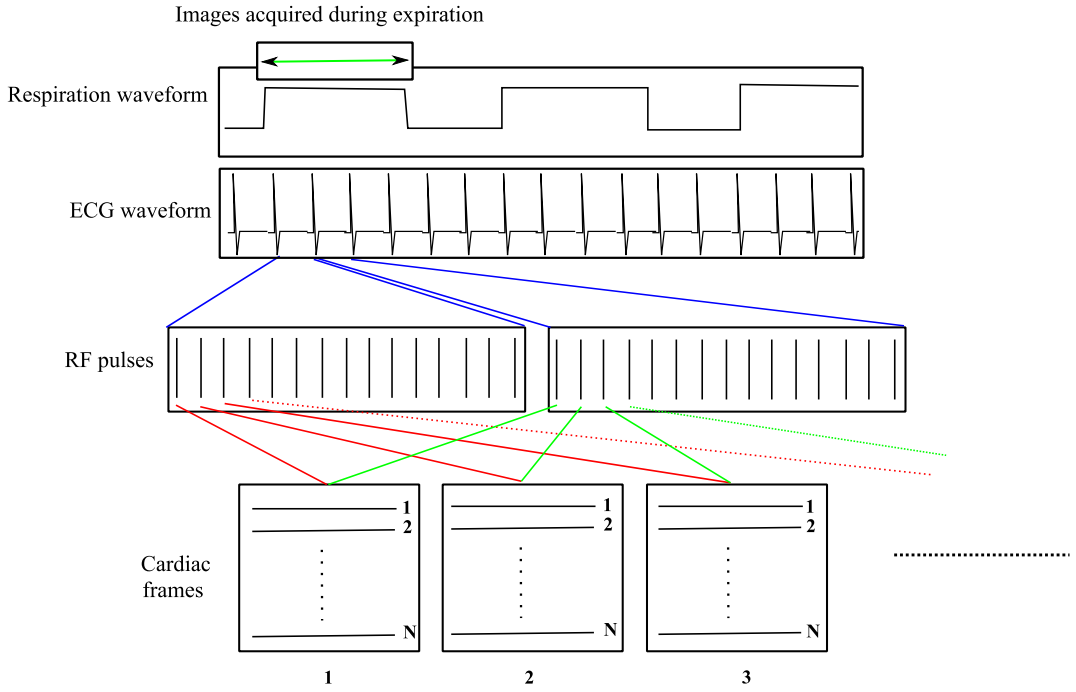

Figure 3.19: Cine imaging using FLASH sequence for functional assessment of the rat's heart. Images only acquired during the expiration period (arrow). Only 1 k-space line was acquired per cardiac frame per cardiac cycle. N_y: phase encoding steps.

3.8 Mock Scan using a Phantom

As described earlier, it is necessary to reduce the dimensions of the coil in order to acquire images with high SNR. To verify this, images of a phantom were acquired using the standard Siemens head coil (Figure 3.20) and our dedicated small-animal birdcage RF coil (Figure 3.1).

The phantom, a bottle with 37 mm in external diameter, filled with saline solution was scanned using the FLASH sequence with parameters: field of view (FOV) = 75 mm, flip angle (α) = 40°, TE = 3.4 ms, TR = 7.4 ms, matrix 320 × 320, pixel bandwidth = 260 Hz/pixel and signal averages = 3. Imaging duration was about 14 seconds.

Figure 3.20: 3T Siemens dedicated head coil with internal diameter of 25 cm.

SNR and relative SNR were measured using the software package available at public domain, called ImageJ ((http://rsb.info.nih.gov/ij, NIH). The mean signal intensity (SI_{ROI}) was measured from within ROI (phantom) and noise was measured as the standard deviation (SD) outside the ROI. The SNR and Relative SNR (expressed as percentage) were assessed as [39]:

$$SNR = {SI_{ROI}}/{SD_{noise}}$$

$$Relative\ SNR = {[SNR_{smallanimal} - SNR_{Headcoil}]}/{SNR_{smallanimal}} \times 100\% \qquad (3.2)$$

3.9 Pilot Scan using Healthy Rats

3.9.1 Animal Preparation

All animal studies were approved by the Faculty of Health Sciences Animal Research Ethics Committee (REC) of the University of Cape Town and performed in accordance with the National Institutes of Health (NIH, Bethesda, MD, USA) guidelines. Five healthy Outbred Wistar Albino rats (weight 227.6 ± 60.26 g (standard deviation)) were used for the pilot study to validate the MRM setup. No surgery was done on these animals. These rats were also used for LV mass (LVM) validation study described in *Part II*.

Following the MRM set up, the heater and the pump were switched on to warm up the cradle. During this time, rats were undergoing preparation for cardiac imaging, as explained below. Physical and physiological monitoring is an important criterion of a cardiac MRM. Isoflurane was used because it is the most effective for immobilizing an animal without significant

effects on cardiac function [55]. Accordingly, rats were initially anesthetized in the induction chamber using 5% isolurane in O_2 flowing at a flow rate of 1.5 L min^{-1} for 5 minutes. After that, subdermal electrodes were attached to the rat's fore and rear limbs, and respiration signals were acquired by coupling one of the ECG cables firmly to the rat's abdomen. Finally, the rat was placed on the cradle, which was already warmed up by the hot water. Using a nose cone integrated on the cradle (Figure 3.5), anesthesia was maintained using 1.5% isoflurane mixed with O_2 at a flow rate of 1.5 L min^{-1}. A rectal temperature sensor was inserted through the rectum to register body temperature. Rats were all placed in the anterior-posterior direction of the magnet. Prior to imaging, the animals were positioned at the isocenter of the magnet with the RF coil in place.

3.9.2 Optimization of Gating Parameters

Figure 3.21 illustrates ECG, respiration and temperature signals acquired from the animal and displayed by PC-SAM. The top window shows the ECG trace as well as heart rate and period of cardiac cycle. The middle window shows breathing rate and period of breathing cycle. The bottom window shows temperature signals, and the current display shows the temperature of the animal is 36.7 °C, which is within the acceptable range.

MRI was triggered only during expiration after detection of the R-wave. Thus, optimization of the gating parameters involved optimizing the R-detect algorithm and setting the thresholds in the breathing signals for gate generation.

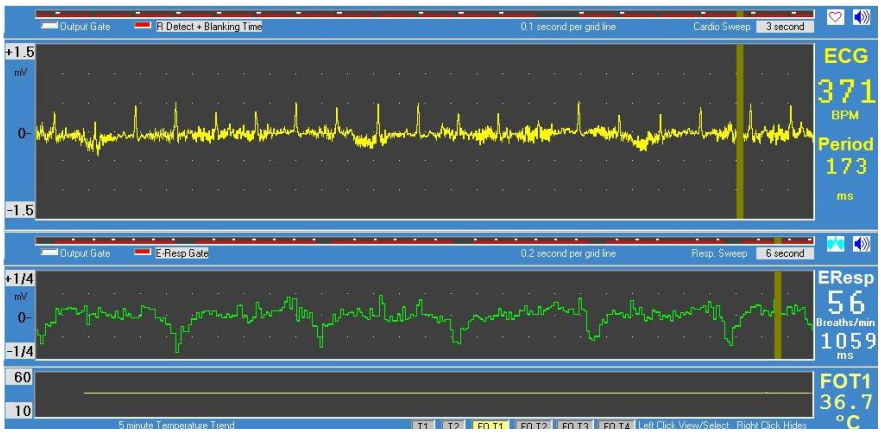

Figure 3.21: ECG signals (top), breathing (middle) and temperature (bottom) signals acquired from a rat.

Although the values of gating parameters mentioned in this section were suitable for most of the animals, minor changes in values were done for few animals due to changes in breathing and ECG signal amplitude.

For ECG gating, a positive peak was chosen for detection of R-wave. In all rats, the rise and fall time chosen for the R-wave were about 6.7 ms and 4.4 ms, respectively, as shown in Figure 3.22. The amplitude of the R-wave chosen for gating was 200 μV as it was large enough to reduce the likelihood of false gates. The maximum amplitude of the R-wave was about 250 μV. Blanking period (Figure 3.23) is one of the most useful features in eliminating false triggers due to gradient vibration. Thus, the blanking period was set to 85% of the R-R period, and the MR scanner acquisition time was set to about 5 to 10 ms below the blanking period depending on the heart rate.

For respiration waveform gates, manual thresholds were applied for different animals. Initially, detection of inspiration period was chosen to simplify the process. Briefly, as shown in Figure 3.23, there are two thresholds (upper and lower) that can be applied to signals. The gate starts when the waveform falls below the lower threshold (107 μV) and ends when the waveform rises above the upper threshold (5 μV). Once the manual thresholds were set to detect inspiration, the pulse was inverted to switch the gate to expiration period.

The blanking period set in the gating parameters was 137 ± 3.5 ms. The variation was due to changes in the heart rate. The upper and lower threshold values of the respiration signal were -42 ± 24 μv and -137 ± 10 μv, respectively. The variations were due to changes in breathing rate and signal amplitude.

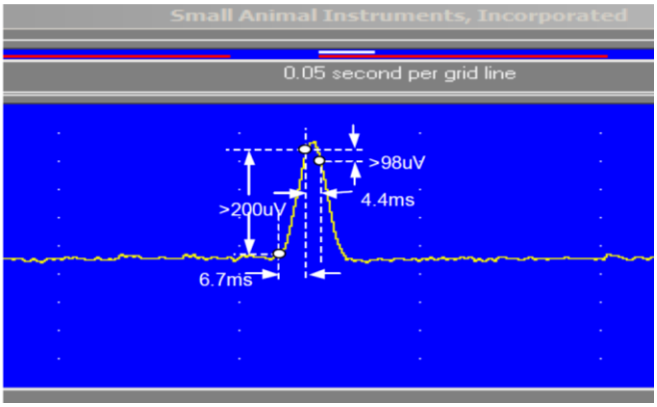

Figure 3.22: Optimizing R-detect algorithm embedded in the SA ECG gating module.

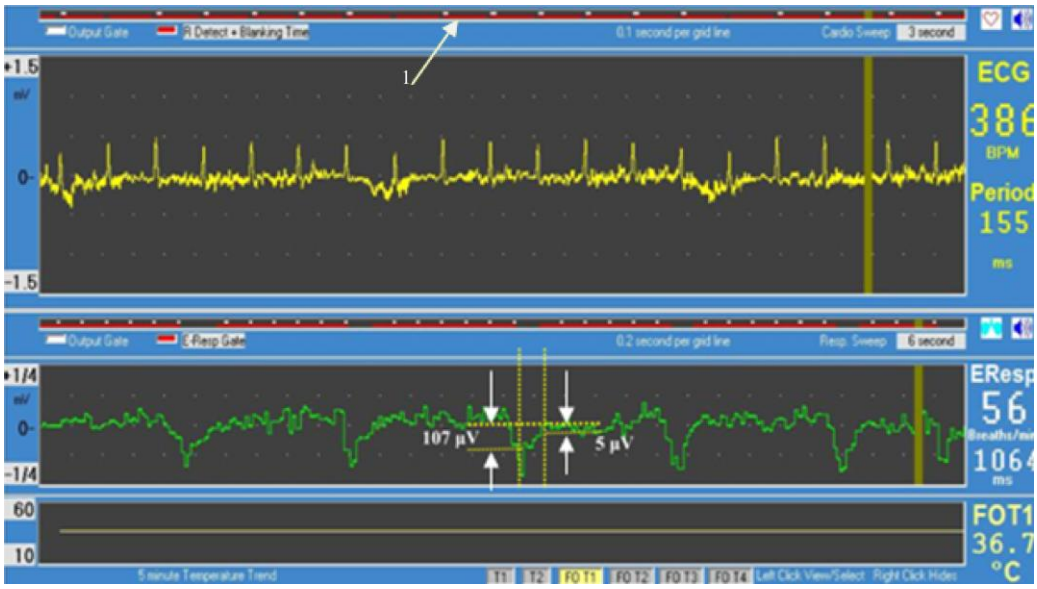

Figure 3.23: Threshold levels specified on respiration waveform. MR scanning starts when the respiration waveform goes beyond 5 µV and stops when it falls below 107 µV. Blanking period illustrated by red line (arrow 1), and the length of the red line describes the percentage of R-R interval prevented from gating incorrectly.

3.9.3 Imaging Protocol

All animals were scanned using a FLASH sequence. Before initiation of cardiac imaging, shimming was performed to reduce magnetic field inhomogeneities. Subsequent to shimming, local coordinate axes of the heart, "long-axis" and "short-axis" were found. The method described by Gilson et al. [12] is the most effective way of determining local coordinate axes of the heart in rodents.

Scout images were used to determine the local coordinate system of the heart. Scout imaging was performed around the rib cage by acquiring multiple slices (axial, sagittal and coronal images) of the heart at low spatial resolution. The number of slices was 10, each with slice thickness of about 1-2 mm. The field of view was about 100 mm, sufficient to encompass the full dimensions of the animal's body. The rest of the imaging parameters were matrix size = 256 × 256, TR = 6.30-7.60 ms, TE = 2.89-3.46 ms and signal averages 1-3 depending on the level of noise.

True long-axis (double-oblique long-axis) images were acquired, as shown in Figure 3.24. Using this image, with ECG gating, the *true* short-axis image was acquired by describing a plane perpendicular to the long-axis image. Figure 3.25 shows the true short-axis image of the

heart. In this project only cine imaging was used to quantify global myocardial function and structure, also regional contractile function.

Figure 3.24: Oblique long-axis image, from which a short-axis image was acquired through a plane perpendicular to long-axis (dashed lines).

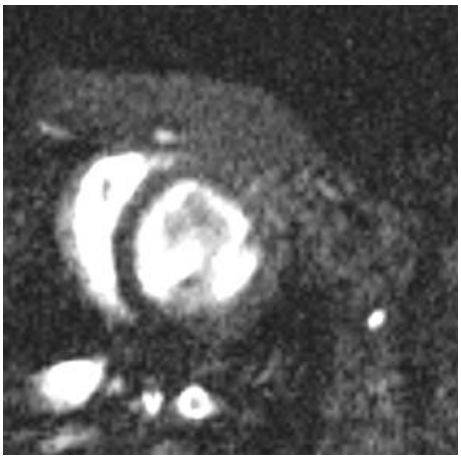

Figure 3.25: True short-axis of the heart acquired from oblique long-axis of the heart with only ECG gating.

Following the determination of local coordinate axes, short-axis images were acquired with the following parameters: field of view (FOV) = 60 mm, matrix size = 256 × 256, in-plane resolution 234 μm, slice thickness 1.0 mm, TR 7.6-8.0 ms, TE 3.44-3.50 ms, flip angle 25^{o} and 40^{o} , bandwidth 282 ± 3 Hz/pixel, and 3 signal averages. The FLASH sequence was triggered by both ECG and respiration. One k-space line was acquired per frame resulting in 16 to 22 frames per cardiac cycle depending on the heart rate.

3.10 SNR and CNR Measurement

SNR, relative SNR and CNR were assessed using the software package ImageJ. Only mid-ventricular ES images, acquired from all healthy animals, were used for these calculations. The mean signal intensity (SI_{ROI}) was measured from within ROI (myocardium (myo) or blood) and noise was measured as the standard deviation (SD) outside the animal's body (Figure 3.26). SNR and CNR of myocardium and LV blood pool were calculated as [39]:

$$SNR = {SI_{myo\ or\ blood}}/{SD_{noise}}$$

$$Relative\ SNR = {\left|(SNR)_{blood} - (SNR)_{myo}\right|}/{(SNR)_{blood}} \times 100\%$$

$$\text{CNR} = \left|SI_{blood} - SI_{myo}\right| / SD_{noise} \times 100\% \qquad (3.3)$$

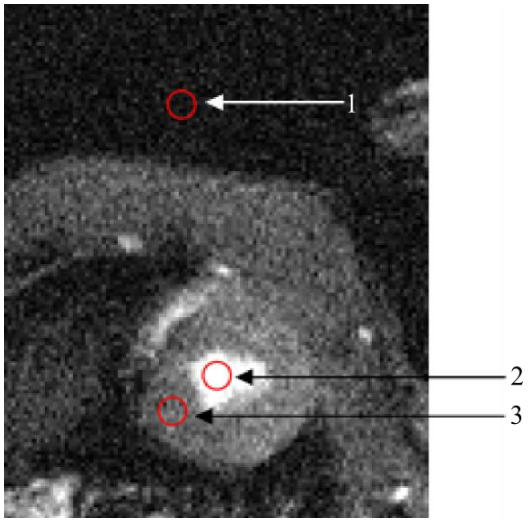

Figure 3.26: Circles describing region of interests in healthy rats. Arrow 1: noise; arrow 2: LV blood; arrow 3: myocardium.

4. Results

4.1 Initial MRM Setup

During the initial MRM setup at CUBIC, the water flow system (water tank, pump and a heater) was connected outside the scanner to assess for any leakages. After a few hours of testing, we found that the system had no leakages or loose connections, and that it could sustain water at a high temperature (50 °C) while flowing at high speed.

An experiment was performed to test the temperature difference between the cradle and water tank. We found that the insulated tubing causes the temperature of the water to drop by less than 2 °C between the two sides.

We scanned a mole rat to determine whether water flow in the cradle causes any artifacts in the image. The resulting image (Figure 4.1) shows that the artifacts do interfere with the ROI. These artifacts were due to turbulence in the flow or non-uniform speed of the water.

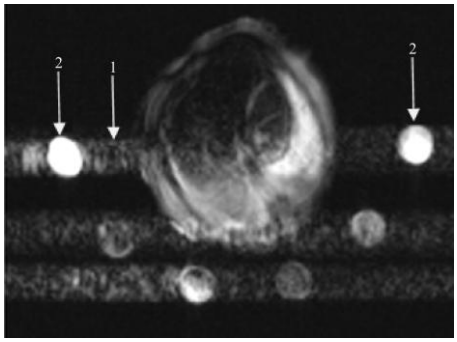

Figure 4.1: MR Image of a mole rat acquired using bSSFP. Flow artifacts were present in the image (arrow 1) which interfered with ROI. We decided to remove first and last loops (arrow 2) to avoid artifacts crossing ROI.

We reduced the number of loops in the flow channel, and using the same mole rat, we found that flow artifacts were far from the rat's body (Figure 4.2). The low-resilience polyurethane (LRPu) foam pillow placed underneath the rat prevents direct contact of the rat with the warm surface of the cradle to further protect the animal (Figure 4.2). In addition, the pillow reduces tossing and turning thus providing better comfort and sleep quality.

During the initial pilot scanning in healthy rats, temperature of water was determined for maintaining the temperature of the rat at 37°C. The resulting temperature was 38 °C which was enough to maintain rat's core body temperature at 37 ± 0.5 °C.

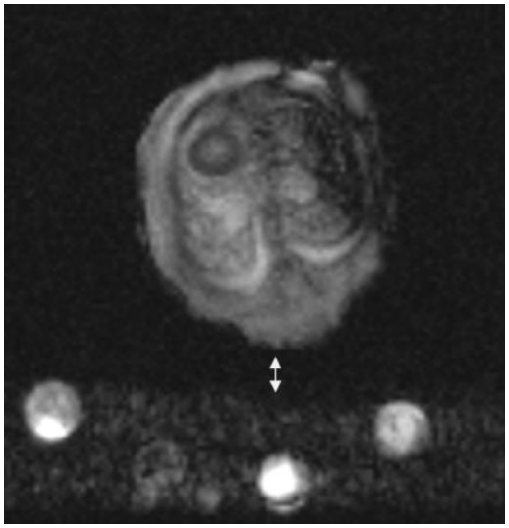

Figure 4.2: MR image of the mole rat after removal of two loops. The posterior surface of the rat was slightly lifted from the cradle to avoid direct contact with the warm surface of the cradle (arrow).

4.2 SNR and CNR measurements

4.2.1 Phantom Studies

A 37 mm bottle filled with saline along with FLASH sequence was used to measure SNR and relative SNR for the two RF coils, Siemens Head coil and small-animal coil. The images of a phantom acquired with the Siemens head coil and small-animal coil are shown in Figure 3.20. Unless stated, the values of SNR and CNR are expressed as mean ± standard deviation (SD) in Table 4.1.

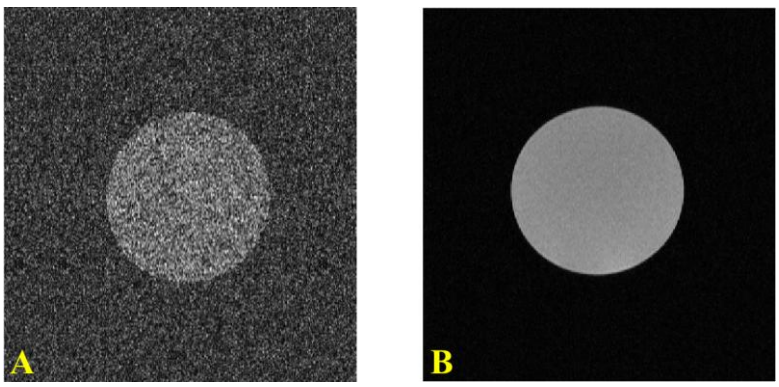

Figure 4.3: Images of phantom acquired using Siemens Head coil (A) and small-animal birdcage coil (B).

The imaging parameters implemented for acquiring phantom images were similar to the parameters used to acquire short-axis images of a rat heart at 4 weeks scan. SI of the ROI (phantom) is significantly higher in the image acquired using small-animal coil (Figure 4.3B) compared to Siemens coil (Figure 4.3A). The resulting SNR and relative SNR (91%) are improved by more than order of magnitude using the small-animal coil compared to the standard Siemens coil (Table 4.1).

Table 4.1: SNR and CNR of the phantom for the two coils

RF Coil	Siemens Head coil	Small-Animal coil
SI_{ROI}	109 ± 45	136 ± 6$^{\#}$
SNR	3 ± 1	42 ± 1$^{\#}$

#P < 0.05 vs Siemens Head coil

4.2.2 Using Healthy Rats

The mid-ventricular ES short-axis images of 5 healthy rats (Figure 3.26) were used to perform SNR and CNR measurements. The results are shown in Table 4.2.

Table 4.2: SNR and CNR measurements of the healthy rat myocardium as well as the LV blood.

ROI	Myocardium	LV blood
SI	100 ± 29	252 ± 9*
SNR	7 ± 2	18.9 ± 0.6*
CNR	11 ± 2	11 ± 2

*P < 0.05 vs myocardium.

Signal of LV blood was significantly higher than myocardium (P<0.05). This resulted in increased SNR of LV blood compared to myocardium. The relative SNR between LV blood and myocardium (58 ± 12%), and the CNR of the LV blood compared to myocardium were also large due to high signal of the blood.

5. Discussion

The aim of this study was to establish a low cost MRM facility for in-vivo cardiac imaging of small-animal models (e.g. rat, mouse) of myocardial infarction. The setup required adaptation of a clinical MRI to performing cardiac MRM. It also entailed construction of a small-animal RF coil and physical support, optimization of the gating system and pulse sequence, and finally validating the MRM setup using healthy rats.

We used a custom built small-animal birdcage RF coil optimized for the dimensions of a rat. SNR and relative SNR measurements of phantom images demonstrate significant improvement in SNR compared to Siemens head coil.

Physical support was built using HDPE, which is non-metallic material and strong. The semi-cylindrical support (cradle) was integrated with a hot water flow system to raise the core body temperature of the animal. A nose cone provided an inlet for supply and maintenance of anesthesia. The cradle offered superb comfort and safety to the animals, as well as a stable and repeatable position. It dissipated heat sufficiently to the animals to raise their core body temperature.

The temperature regulation system maintains the temperature of the rats at 37 ± 0.5 °C. This range of core body temperature is in agreement with previous studies conducted on rodents [50,64-66]. No burn marks were observed on rats, suggesting absence of hot spots in the cradle due to adequate flow of water in the cradle. Although the water flow system caused artifacts in the image, it did not interfere with our ROI, thus facilitating accurate visual and quantitative (described later) analysis of cardiac images.

The body temperature of some rats dropped to about 35°C due to effects of anesthesia [44]. While the temperature increased slowly to the target value (37°C), large variations in heart beat were observed, causing substantial increment in imaging time. To reduce the scan time, the MR acquisition window (time) was reduced to a level that did not affect imaging major cardiac phases (ED and ES).

The cardiac and respiratory gating system was optimized to suite rat physiology allowing cardiac images to be acquired with excellent SNR of myocardium (7 ± 2) and LV blood (18.9 ± 0.6). The significantly higher signal of blood, compared to myocardium, results from the

large flip angle chosen to maximize the signal intensity of flowing blood relative to the surrounding stationary tissue that has become saturated by repetitive RF pulses [67].

Part II: Application of MRM to Study Animal Model of LVR in Non-Reperfused MI

6. Background and Literature Review

6.1 Rodent Model of Myocardial Ischemic Disease

6.1.1 Background

In cardiovascular research, rodent (mice and rats) models have been used to study chronic heart failure in different stages of cardiovascular diseases, such as myocardial ischemic disease [68]. Rodent models are preferred over large animal models because of their small size, easy availability and low maintenance cost. Furthermore, the advent of transgenic and gene knockout technologies have allowed a generation of rodents that mimic human cardiovascular diseases [69].

6.1.2 Techniques

Myocardial ischemia arises when there is an inequality between myocardial oxygen supply and consumption due to a decline in coronary blood flow, which if not restored rapidly would lead to infarction of myocardium [19]. Various techniques have been implemented to induce myocardial ischemia, such as coronary artery ligation [70], microembolism [71] and ameroid constrictors [69]. However, ligation of the left anterior descending coronary artery (LAD) is the most simple, reproducible and preferred method of inducing myocardial infarction (MI) [72]. It is done either by placing a silk suture around the LAD and surrounding myocardium (Figure 6.1) of the left ventricular (LV) wall [70] or by burning the myocardium surrounding the LAD [73]. The resulting infarcts from the later technique are usually comprised of epicardial burns surrounded by small areas of infarction making it difficult to perform accurate infarct size measurement [73].

Rat models of heart failure are widely and successfully used and are preferred over mouse models because of reasons explained by Patten et al. [72]: it is easier to perform open-chest surgical procedures and invasive hemodynamic assessments, and a greater number of

postmortem histological or molecular biological analyses can be done given the approximately 10-fold greater myocardial mass of rats compared with mice.

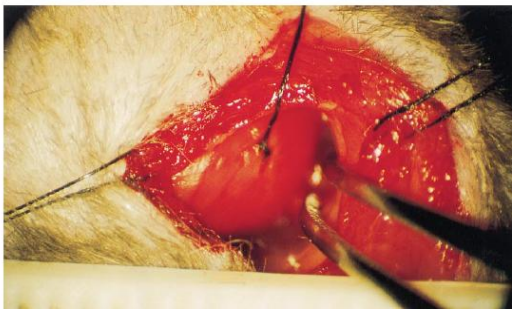

Figure 6.1: A mouse undergoing coronary artery ligation as seen through surgical microscope [70].

6.1.3 Rat Model of Non-Reperfused Myocardial Infarction

Rat models of non-reperfused MI have been widely used to examine left ventricular remodeling (LVR) and performance after the induction of myocardial infarction (MI) [74]. In addition, the effects of drug therapy, such as angiotensin converting enzyme (ACE) inhibitor and beta-adrenergic blocking agents have been examined using this model [75-76]. Most of these studies are conducted over the period of 4 weeks to characterize the short-term LVR in the rat model *because* during this period major changes in cardiac function and structure are completed, including myocardial necrosis, fibrosis and remodeling [77]. These models are examined histologically, preventing any further investigation in the same animal, thus leading to a large number of animals required for experiments [73]. Therefore, it is imperative to have *non-invasive* methods to accurately characterize LVR post MI, providing subject-specific longitudinal data and reducing the number of animals needed.

6.2 Image Analysis

Data analysis is necessary to compute functional and structural parameters. These parameters can be calculated at a single time point or at several time points required to study disease progression or response to intervention therapy. Standard functional and structural parameters can be assessed by outlining endocardial and epicardial borders in cine cardiac images (Figure 6.2). Such parameters include end-diastolic volume (EDV), end-systolic volume (EDV), stroke volume (SV), ejection fraction (EF) and LV mass (LVM).

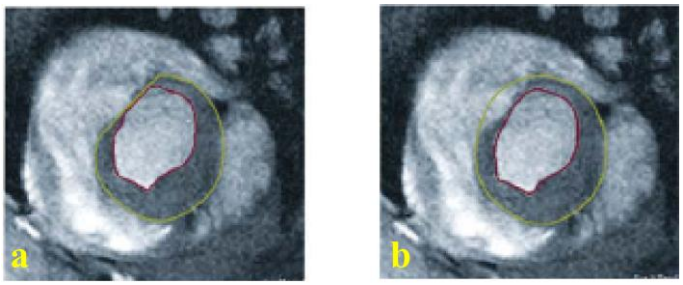

Figure 6.2: Myocardial short-axis image segmentation. Green line delineates epicardial border while red line delineates endocardial border. Segmentation with (a) without long-axis correction and (b) with long-axis correction [78].

Data analysis can be performed using manual segmentation software, such as ImageJ (NIH, http://rsb.info.nih.gov/ij) and CAAS-MRV FARM (version 1.0, Pie Medical Imaging, Maastricht, The Netherlands). These segmentation methods yield accurate results with low inter-observer and intra-observer variability [78-79].

Due to the time consuming nature of manual segmentation, freely available semi-automatic segmentation software (SASs), such as CMRTools (http://www.cmrtools.com) and Segment (http://segment.heiberg.se), have been developed and provide accurate results. Similar to manual segmentation, semi-automatic segmentation methods have also been shown to have low inter-observer and intra-observer variability [41,78]. These methods use different approaches that range from simple thresholding and edge detection to very advanced deformable models for volume estimation, and usually include long-axis views for valve definition accuracy [28,80].

6.2.1 Myocardial Mass

Left ventricular myocardial mass (LVM) is an important measure in patients suffering from cardiovascular diseases, such as cardiomyopathy, hypertension and valvular disease [19]. In-vivo cardiac MRI has the ability of quantifying accurately LVM due to its ability to offer high spatial resolution with high CNR between myocardium and LV blood [20]. LVM is calculated from a stack of images covering the whole heart. Briefly, segmenting endocardial and epicardial borders of the LV, and considering the out-of-plane resolution, results in myocardial volume. Multiplying this volume by myocardial tissue density (1.05 g cm^{-3}) yields the LVM [12,28]. In-vivo quantification of LVM using non-clinical MRI scanners has been validated in rats and mice [26,43,81].

6.2.2 Myocardial Function

Cardiac MRI has become the gold standard for measuring global and regional myocardial function in humans and animals [28,40,43,82-83]. Global myocardial function is calculated from a stack of cardiac images covering the whole heart. For each slice and each cardiac phase in the short-axis image stack, the endocardial borders are outlined, after which the segmented areas when multiplied by slice thickness results in LV chamber volumes. The largest ventricular volume of the slice is the end-diastolic volume (EDV) prior to systolic contraction, while the smallest one is end-systolic volume (ESV) [12].

During segmentation, some previous studies considered papillary muscles as part of the LV blood pool (not part of myocardium) [84-86]. This approach has been adopted due to its simplicity, as the shape of the LV blood pool is made much simpler, thus making the evaluation of LV volume faster and more time efficient [87]. However, omission of papillary muscles causes significant differences in measurements of EDV and ESV, but not in EF [87]. Nonetheless, possible effects of omitting papillary muscles should be taken into account when performing data analysis, especially during estimation of ESV [78].

Cardiac images acquired using clinical grade scanners suffer from reduced signal and contrast due to lower field strength [19]. Consequently, high resolution images (< 250 μm in-plane resolution) acquired in clinical scanners with gradient echo (GE) sequences generally result in poor definition of the endocardial and epicardial boundaries, requiring manual intervention during the segmentation process [22]. This study evaluates whether 3T clinical MRI with a small-animal coil and optimized GE sequence could generate images with sufficient contrast and resolution to characterize using semi-automatic segmentation software (SASs) short-term LV remodeling (LVR) and changes in functional parameters – such as LV EF, EDV and ESV – following induction of non-reperfused MI in rats.

7. Methodology

7.1 Animal Model and Preparation for Cardiac MRM

7.1.1 Surgery

All animal studies were approved by the Faculty of Health Sciences Animal Research Ethics Committee (REC) of the University of Cape Town and performed in accordance with the National Institutes of Health (NIH, Bethesda, MD, USA) guidelines. 12 male Outbred Wistar Albino rats were used for the study (weight 195.3 ± 10.8g (standard deviation) at implant).

The animals were split into two groups namely; sham (n = 5) and MI (n = 7). In the MI group, a non-reperfused MI was induced as previously described by Dobner et al. [88]. Briefly, rats were placed in an induction chamber and anesthetized with air flow containing 5% isoflurane and 1.5% Oxygen. Animals were then intubated with a 16G catheter and mechanically ventilated with 1.5-2% Isoflurane and 0.3% Oxygen. A left intercostal thoracotomy was performed and MI was induced by permanent ligation of the left anterior descending (LAD) coronary artery. A 6-0 prolene suture was used to ligate and placed 2 to 3 mm below the left atrial appendix. Fibrillation and ischemia of the LV wall confirmed the infarction. Sham animals were subjected to the same procedure without ligation of LAD coronary artery. Following the surgical procedure, an analgesic dose of 100 µl Temgesic was administered by intramuscular injection to the hind leg. Animals were monitored daily for the duration of the study. Analgesic (100 µl Temgesic) was administered every morning for 3 days after surgery. All animals survived surgery.

7.1.2 Gating Parameters

In the sham group the gating parameters were similar to the ones implemented in healthy rats. In the MI group, similar to the previously reported study [29], the abdominal thinning and a reduction of physical strength, greatly affected ECG gating stability. The falling edge was then used for detection of R-wave as it was the only option that worked well in these animals. In the attempt to further *reduce* noise levels in the cardiac images, the ECG cables and ECG/Temperature module were taped firmly to the MRI bed to eliminate unwanted movement from gradient vibration.

7.1.3 Imaging Parameters

Only single slice acquisition was done for long-axis images, and its MR parameters were: field of view (FOV) between 60-100 mm, matrix size = 256 × 256, in-plane resolution 234 to 390 µm, slice thickness 1.0-2.0 mm, TR 6.3-7.7 ms, TE 2.89-3.46 ms, flip angle 40^{o} , and 3 signal averages.

MR parameters for short-axis images were: field of view (FOV) = 60 mm, matrix size = 256 × 256, in-plane resolution 234 µm, slice thickness 1.0 mm, TR 7.7 ms, TE 3.5 ms, flip angle 25^{o} -40^{o} , bandwidth 300 Hz/pixel, and 3 signal averages. For the four week scan, FOV and matrix size were increased to 75 mm and 320 × 320, respectively, and the bandwidth was reduced to 260 Hz/pixel. In all cases, the FLASH sequence was triggered by both ECG and respiration. One k-space line was acquired per frame resulting in 18 to 30 frames per cardiac cycle depending on the heart rate. 3 signal averages were implemented to yield adequate SNR. Acquisition time was approximately 2.5 minutes per slice, and 15 to 16 slices were typically required to cover the entire LV. One to two additional slices were acquired to cover the entire LV of the MI group at the 4^{th} week scan due to animal growth.

7.2 MR Image Analysis

7.2.1 Image Segmentation

Only short-axis images were used for functional and structural analyses. The image stacks with largest LV cavity were used as the end-diastolic (ED) images and the smallest as end-systolic (ES) images. From ED and ES short-axis images, LV borders were segmented using SASs, called Segment (http://segment.heiberg.se) without any long-axis correction. This software has been shown to yield low inter- observer and intra-observer variability (< 5%) in volumetric analyses [78]. We implemented the LV segmentation technique and definitions for the most apical and basal slice that were previously explained by Riegler et al. [78]. Briefly, the most apical slice is defined as the first slice with no blood pool while the most basal slice is the one that shows a remaining part of the thick myocardium and is below the aortic valve. Papillary muscles were segmented as part of the myocardium (Figure 7.1A and B) as they contribute considerably to the blood pool at end-diastole [19].

Analyses using Segment software was initiated using the ‘‘left ventricular tool’’ algorithm. First, a marker was positioned in the center of the LV blood pool, from which the algorithm

fits a deformable model that expands toward the endocardial border to include the LV blood pool across the various short-axis slices. Afterward, manual corrections were performed as necessary for the epicardial border, and for the endocardial border where the papillary muscles appeared separated from the myocardium. If the myocardium moved out of the plane due to long-axis contraction, a straight line was drawn to merge the two visible ends of the myocardium (Figure 7.1C), as described by Barbier et al. [89].

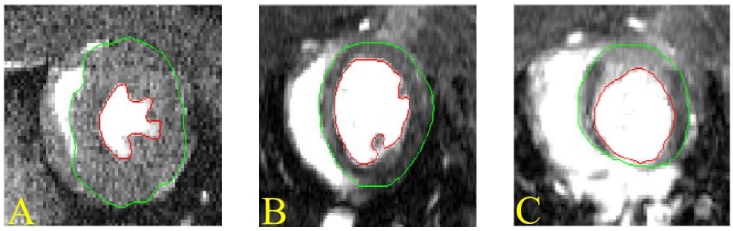

Figure 7.1: Myocardial segmentation. Green line marks the epicardial border while the red line marks endocardial border. ES (A) and ED (B) images illustrate papillary muscles segmented as part of myocardium. The last image (C) illustrates the straight line used to connect the two ends of the myocardium.

7.2.2 Global and Regional Functional Analysis

Subsequent to the segmentation process, EDV, ESV, and LV mass (LVM) were measured by SASs. Other functional parameters were calculated as follows; stroke volume (SV) = EDV – ESV, EF = 100 × SV/EDV and cardiac output (CO) = SV × Heart Rate.

LV wall thickness (WTh) was measured 2 and 4 weeks post surgery using the same software. WTh analyses were performed on mid-ventricular slices as explained by Ross et al. [26] and Ojha et al. [66]. Briefly, following the delineation of epicardial and endocardial borders, the LV wall was divided into 16 equal sectors using the right anterior ventricular insertion as a reference point. 4 contiguous measurements were averaged to form 4 equal sectors of 90^{o} each. These four sectors were called Anterior (0^{o}-90^{o}), Lateral (90^{o}-180^{o}), Posterior (180^{o}-270^{o}) and Septal (270^{o}-0^{o}), as shown in Figure 7.2. Papillary muscles were not included in this analysis. Subsequent to wall thickness measurements, %systolic wall thickening (%WTh) was calculated as 100 × (systolic wall thickness – diastolic wall thickness) / diastolic wall thickness.

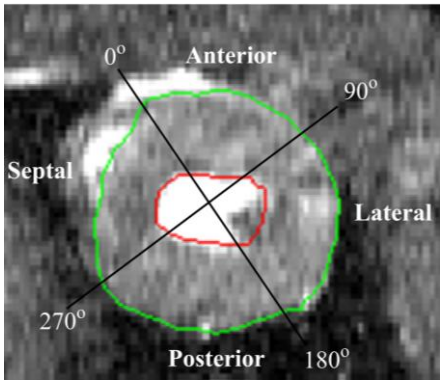

Figure 7.2: LV wall averaged into 4 equiangular segments 90° sectors after myocardial segmentation.

7.2.3 SNR and CNR Measurement

SNR, relative SNR and CNR were assessed using the software package ImageJ. Only mid-ventricular ES images, acquired at four week scan, were used for these calculations. Images of all animals were used in these analyses. The SNR, relative SNR and CNR measurements of myocardium and LV blood in these rats were performed in the same manner described earlier in healthy animals.

7.3 Histological Preparation and Infarct Size Measurement

A day after the completion of MRI scanning all animals were euthanized with intraperitoneally injected sodium pentobarbitone whilst under isoflurane induced anaesthesia. Hearts excised from healthy rats were trimmed free of right ventricle and atria to determine true LV mass. In the MI group, infarct size was determined histologically as described by Dobner et al. [88]. Briefly, the hearts were injected with 1 ml ice cold saturated KCl solution after anaesthesia to arrest them in diastolic state and then excised for weighing. 3 µm sections were obtained from 4 equal divisions of every heart. Each section was stained with Masson´s trichrome to determine the extent of infarction and images were captured with a Nikon E1000 M camera (Nikon, Tokyo, Japan) with a 0.5X magnification lens. Infarct size was determined using the midline method as previously described by Takagawa et al. [90]. Briefly, infarct size was measured as the sum of midline length of infarcted myocardium from all sections divided by the sum of midline LV circumferences from all sections multiplied by 100. Measurements were acquired with Visiopharm Integrator Systems (Visiopharm, Hørsholm, Denmark).

7.4 Statistical Analysis

If not indicated otherwise, all data are specified as mean ± standard error of the mean (SEM). Correlation and Bland-Altman analyses [91] were used to examine the relation and agreement between MR LVM and post-mortem measurements. An unpaired two-tailed t-test was used to compare LV function and mass between sham and MI groups, and a paired t-test was used to compare MI groups at different time points. $P < 0.05$ was considered significant.

8. Results

8.1 SNR and CNR Measurements Using Sham and MI Rats

The mid-ventricular ES images of all rats were used to perform SNR and CNR measurements. SNR of myocardium and LV blood in sham rats was higher than in MI rats ($p < 0.05$). Similarly, CNR of LV blood compared to myocardium in sham rats was significantly higher than in MI rats ($p < 0.05$). Disparity observed in SNR and CNR between the groups are ascribed to the low levels of artifacts observed in sham rats compared to MI rats.

Subsequent to aforementioned comparison, the collective average SNR and CNR of myocardium and LV blood were determined. The results are shown in Table 8.1.

Table 8.1: SNR and CNR measurements of the rat myocardium as well as the LV blood expressed as mean ± standard deviation

ROI	Myocardium	LV blood pool
SI	92 ± 20	254 ± 4*
SNR	12 ± 4^{+}	32 ± 8$^{*,+}$
CNR	21 ± 5	21 ± 5^{+}

*P < 0.05 vs myocardium, +P < 0.05 vs corresponding SNR/CNR in healthy rats.

Similar to the healthy rats, signal of LV blood was significantly higher than myocardium ($P<0.05$). SNR of LV blood is 64% higher than in myocardium.

SNR was significantly higher in sham and infarcted rats than in healthy rats (7 ± 2 for myocardium and 18.9 ± 0.6 for LV blood, respectively, as shown in Table 4.2) due to optimized sequence parameters, lower bandwidth, and greater number of phase encoding steps.

8.2 Image features

In this study, single and multiple slice acquisition of long-axis and short-axis cardiac images, were performed in every rat. The image contrast and resolution in this study were sufficient to delineate major anatomical landmarks. Figure 8.1A shows a 4 chamber long-axis image of the rat heart that depicts the four chambers of the heart. Figure 8.1B shows a short-axis image of

rat heart. The short-axis image shows the right and left ventricles of the heart. Left and right ventricular walls (lvw and rvw) surrounding the left and right ventricles, respectively, are clearly visible. Papillary muscles are also visible, making it possible to perform accurate volumetric analyses [19]. In every rat, a stack of short-axis images covering the whole heart was captured and used for image analyses.

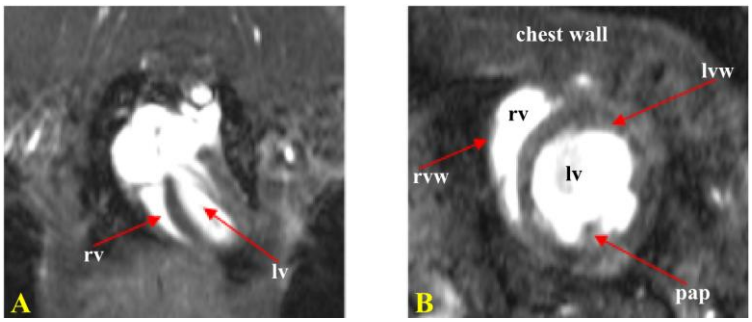

Figure 8.1: Two standard orientations of cardiac images. A) 4 chamber long-axis and B) short-axis images. Major anatomical landmarks are also described using arrows. lv: left ventricle, rv: right ventricle, lvw: left ventricular wall, rvw: right ventricular wall, pap: papillary muscle.

8.3 LV Mass Authentication

Healthy rats were used to validate MR LV mass with the true wet LV mass found by measurement on an electronic weight balance a day after pilot imaging. The mean MR LV mass was 512 ± 32 mg, while the mean wet LV mass was 510 ± 28 mg, correlation 0.87. Bland-Altman analysis revealed a mean difference of 2 mg between the two methods with 95% confidence interval of 72 mg, as shown in Figure 8.2.

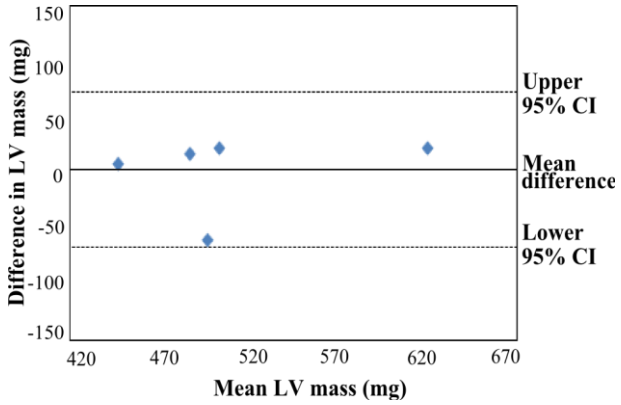

Figure 8.2: Bland-Altman analysis showing agreement between MR measurement and post-mortem measurements of LV mass in healthy rats. The analysis revealed mean difference of 2 mg (solid line) and 95% confidence interval of 72 mg (mean difference ± 1.96 × SD). CI: confidence interval.

8.4 Structural and Global Functional Analysis

Long-axis images at ES phase acquired at 4 weeks after surgery illustrate the extent of LVR induced by large MI (Figure 8.3). The mid-ventricular short-axis images (Figure 8.4) at ED and ES acquired from sham and infarcted rats at 2 and 4 weeks after surgery illustrate dilation and wall thinning in anterior and lateral regions of the heart. Dilation of ESV is evident by 2 and 4 weeks after surgery demonstrating contractile dysfunction (Figure 8.3 and Figure 8.4).

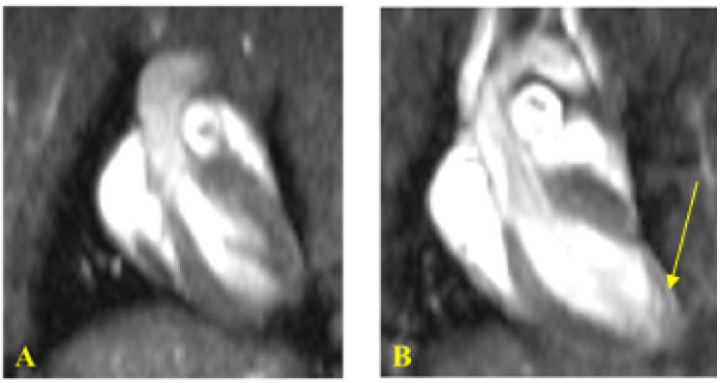

Figure 8.3: Long-axis ES MR images of rat heart. A) Sham rat and B) MI rat acquired 4 weeks after surgery. Significant wall thinning (arrow) and dilation is apparent in the anterolateral LV wall towards the apex of the heart. LVR has taken place to increase LVESV.

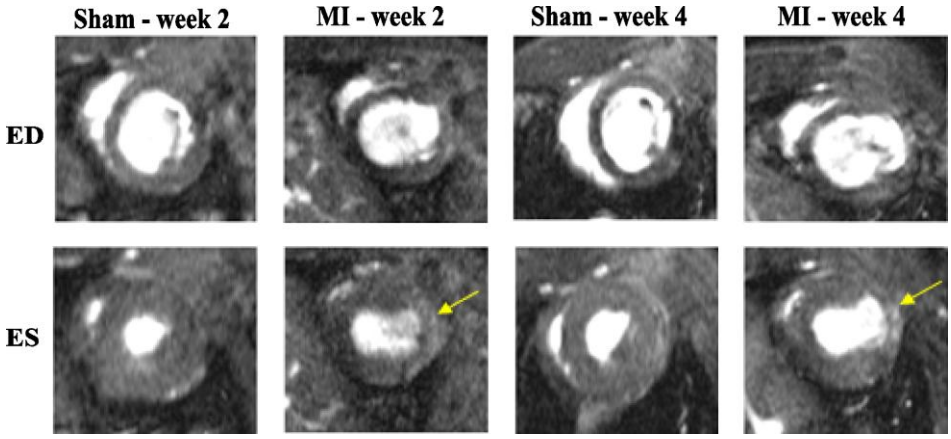

Figure 8.4: Short-axis images of the heart from sham and MI rats. Top row shows ED images 2 and 4 weeks post surgery and bottom row same for ES. ES images demonstrate significant dilation and wall thinning (arrows) in MI group at 2 and 4 weeks post surgery.

Figure 8.5A shows a Masson's trichrome stained slice from an infarcted rat illustrating the extent of infarction and wall thinning in anterior and lateral regions of the heart. Figure 8.5B shows a hematoxylin-eosin stained slice from an infarcted rat demonstrating loss of myocytes.

Figure 8.5C shows Masson's trichrome stained slice from a sham rat with no infarction. Figure 8.5D shows hematoxylin-eosin stained slice illustrating correct alignment of myocytes in absence of infarction. From post-mortem measurements, infarct size was found to be 27 ± 3%. Table 8.2 describes cardiac parameters of sham and MI animals post surgery.

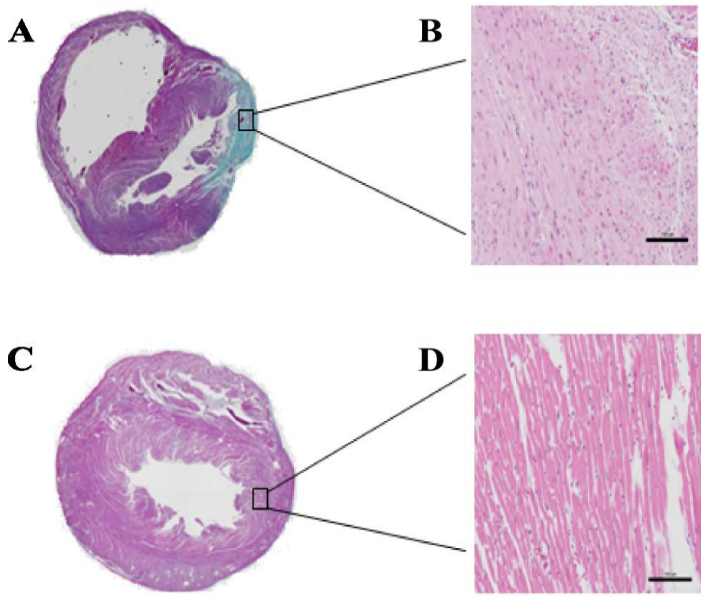

Figure 8.5: Comparison of histological images 4 weeks post surgery for an MI rat (A,B) and a sham rat (C,D). A: Myocardial tissue slice of MI rat – Scarred tissue (collagen) is very prevalent in the infarcted area in the anterior and lateral regions of the heart (as indicated by blue stain). Significant wall thinning is evident in infarcted areas. B: Hematoxylin-eosin stained slice from an infarcted rat x10 magnification (scale bar = 100 µm). Loss of myocytes is evident in the infarcted area which is rich with atypical nuclei. C: Myocardial tissue slice of a sham rat. There is no evidence of scarring. D: Hematoxylin-eosin stained slice from a sham rat x10 magnification (scale bar = 100 µm). Appropriate alignment and no loss of myocytes indicate absence of infarction.

At 2 weeks post surgery, EDV did not increase significantly (Figure 8.6A), while there was significant increase in ESV in the MI group (Figure 8.6B) compared to the sham group ($p < 0.05$). There was no significant change in CO and SV at 2 and 4 weeks post surgery. At 4 weeks post surgery, there was significant enlargement of EDV and ESV in the MI rats compared to sham rats at 4 weeks post surgery ($p < 0.05$). For the MI group, EF dropped significantly at 2 weeks and further considerable drop was observed at 4 weeks post surgery (Figure 8.6C). LVM was significantly greater in MI rats compared to sham rats both at 2 and 4 weeks post surgery (Figure 8.6D). The LVM in infarcted rats did not significantly increase between 2 (664 ± 27) and 4 (712 ± 16) weeks post surgery, as shown in Table 8.2.

Table 8.2: LV Global Parameters

	Week 2		Week 4	
Group	**Sham**	**MI**	**Sham**	**MI**
EDV (µl)	426 ± 22	488 ± 56	443 ± 18	624 ± 63$^{*, \dagger}$
ESV (µl)	104 ± 9	189 ± 22*	121 ± 9	299 ± 41$^{*, \dagger}$
SV (µl)	322 ± 16	299 ± 36	322 ± 12	326 ± 29
CO (ml/minute)	112 ± 7	105 ± 12	119 ± 5	123 ± 12
EF %	76 ± 1	61 ± 2*	73 ± 1	53 ± 3$^{*, \dagger, +}$
True heart weight (g)			1.2 ± 0.1	1.5 ± 0.1†
LVM by MRI (mg)	600 ± 21	664 ± 27*	615 ± 10	712 ± 16$^{*, \dagger}$

*P < 0.05 vs week 2 sham, †P < 0.05 vs week 4 sham, +P < 0.05 vs week 2 MI.

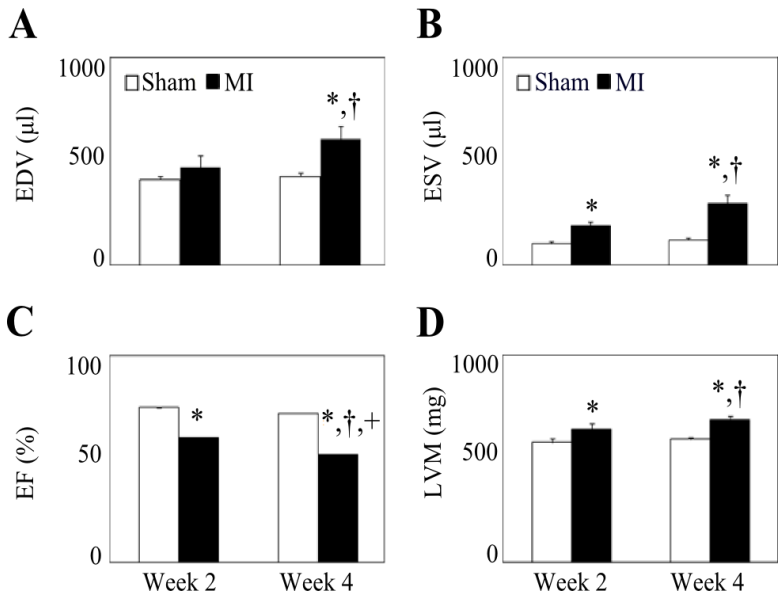

Figure 8.6: Average LV functional parameters and LVM determined by MRI. In the MI group, EDV (A) and ESV (B) were significantly higher at 4 weeks. ESV was also higher at 2 weeks compared to sham rats. EF (C) was significantly lower at both 2 and 4 weeks. LVM (D) was significantly higher at 2 weeks and 4 weeks in MI rats indicating hypertrophy. *p < 0.05 vs week 2 sham, †p < 0.05 vs week 4 sham, +p < 0.05 vs week 2 MI.

8.5 Regional Functional Analysis

The MI group revealed dyskinesia and severe wall thinning in the infarcted area (Figure 8.3 and Figure 8.4) at 2 and 4 weeks post surgery. In order to quantify this, we performed WTh analyses on a mid-ventricular slice at 2 and 4 weeks post surgery in the MI and sham rats by dividing their mid-ventricular short-axis images into 16 equal sectors. 4 contiguous measurements were averaged to form 4 equal sectors of 90° each.

8.5.1 2 weeks post surgery

WTh at ED in the MI group showed minor increase in thickness in all regions of the heart (Figure 8.7A). However, at ES, modest decrease were observed in the infarct region (anterior and lateral), as illustrated in Figure 8.7B. The summation of changes at ED and ES led to reduced wall thickening in all sectors of the heart, as shown in Figure 8.7C.

8.5.2 4 weeks post surgery

At ED in the MI group, there was a significant drop in wall thickness in the anterior region, and a modest decrease in the lateral region (Figure 8.8A). In addition, in the posterior region there was significant increase in wall thickness while there was modest increase in the septal region. Increases in the posterior and septal regions indicate the presence of hypertrophy. At ES in the MI group, we observe a significant drop in wall thickness in the anterior and lateral regions (Figure 8.8B), while there was a modest decrease in wall thickness in posterior and septal regions. Histological analysis of the MI group revealed complete absence of scar tissue in the septal region (Figure 8.5A). In contrast, most of the anterior and lateral quadrants of the heart demonstrate the presence of scar tissue and severe wall thinning (Figure 8.5A)**.** These two quadrants suffered severe contractile dysfunction as a result of MI, as evident from the significantly reduced wall thickening during systole (Figure 8.8B). MI rats demonstrated reduction in systolic wall thickening in all regions of the heart. Reductions were significant in lateral and posterior regions (Figure 8.8C).

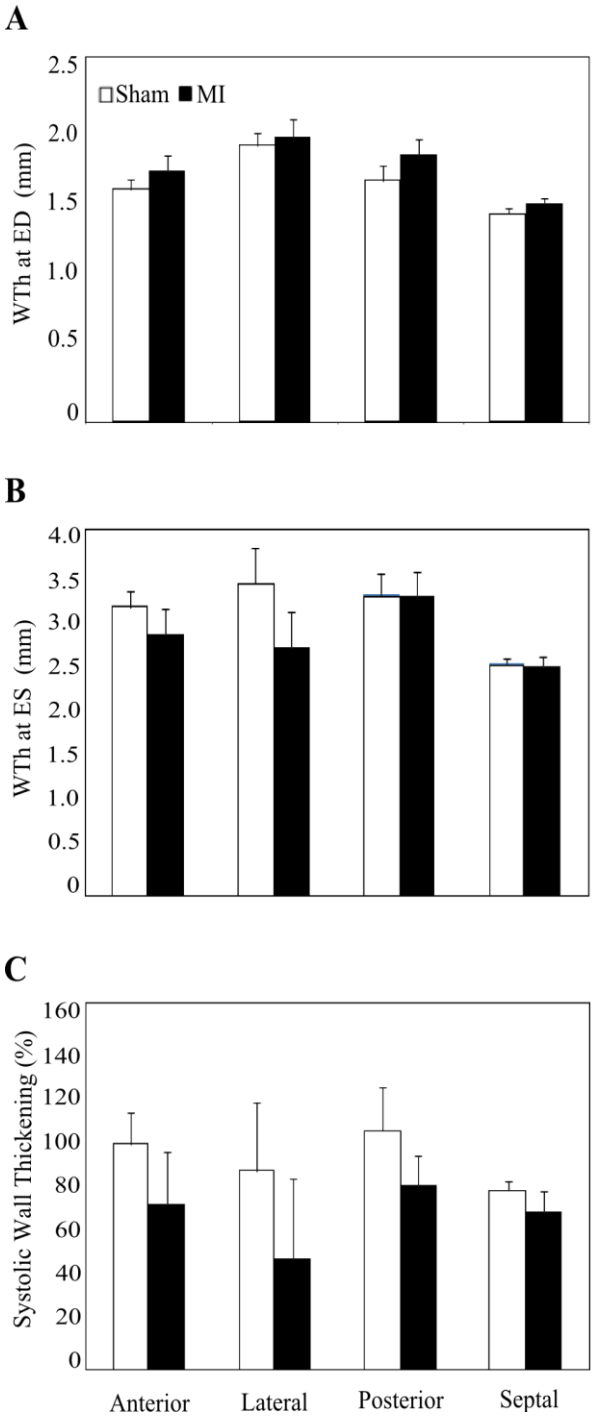

Figure 8.7: Analyses of regional LV function 2 weeks post surgery. A) Modest increase in all regions of the heart at ED. B) Modest changes were observed at ES in anterior and lateral. C) All segments of the heart show modest reduction in systolic wall thickening.

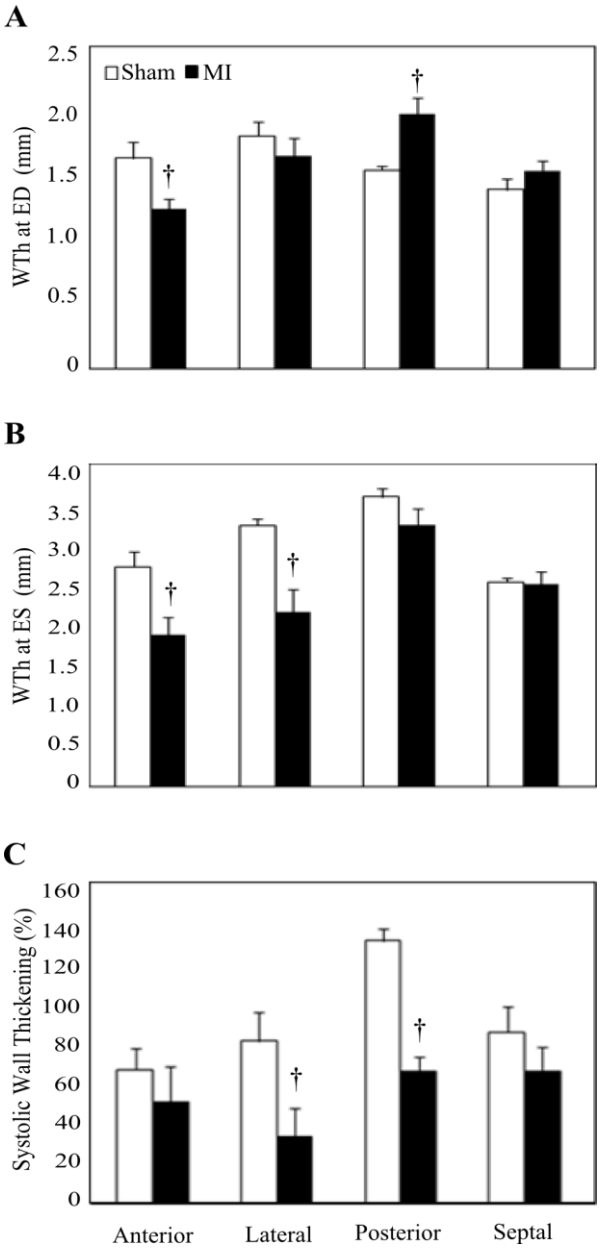

Figure 8.8: Analyses of regional LV function 4 weeks post surgery. Significant wall thinning occurs at ED in antero-lateral regions while the posterior region demonstrates significant wall thickening (A). At ES, significant wall thinning is observed in anterior and lateral regions, while a modest decrease is evident in the posterior region (B). While all four regions show reduction in systolic wall thickening, it is only significant in the lateral and posterior regions (C). †$p < 0.05$ vs week 4 sham.

9. Discussion

9.1 SNR and CNR in Sham and MI Rats

Similar to the healthy rats, the cardiac and respiratory gating system allowed cardiac images to be acquired with excellent SNR of myocardium (12 ± 4) and LV blood (32 ± 8).

The noise levels in the sham and infarcted images were significantly lower than in healthy animals. This was due to reduction of receiver bandwidth (Equation 2.4) from 282 ± 3 Hz/pixel (for healthy rats) to 260 Hz/pixel, and also due to increase in-phase encoding steps (Equation 2.4) from 256 to 320 steps [45]. At 2 and 4 weeks scan, ECG cables and ECG/Temperature module were firmly fixed to the MRI bed to prevent any movement from gradient vibrations. This probably aided in reducing the noise levels in the cardiac images.

Considerable increase in LV blood and myocardium signal, and reduction in noise levels led to significant increase in their SNR and CNR of LV blood compared to myocardium, making it possible to perform visual and quantitative analysis.

9.2 FLASH Sequence for Cardiac Imaging

The implementation of the optimized FLASH sequence parameters yielded images with sufficient SNR and CNR to delineate major anatomical landmarks, such as papillary muscles. In addition, these parameters produced images within reasonable scan times with excellent isotropic spatial in-plane resolution, 234 μm and 1 mm slice thickness, which were higher than reported resolution with non-clinical scanners [27-28]. This resolution enabled accurate visual and quantitative WTh analyses, thereby providing extra information and better understanding of LVR in the rat heart. The temporal resolution (7.7 ms) was also higher than previously reported values with clinical and non-clinical scanners [21,23,29,66]. This resolution resulted in a large number of frames per cardiac cycle which improved the volumetric analyses.

9.3 Image Segmentation with Segment

The contrast between LV blood pool and myocardium (56 ± 6%) was large enough to effectively use SASs for segmentation to evaluate cardiac parameters. We compared our EF values, a major determinant of cardiac function, with reported values in the manner explained

by Riegler et al. [78] and Delattre at al. [23]. In our study, EF in healthy animals (71.8 ± 1.3%) was equivalent to reported values [27,92]. Similarly, EF in sham rats showed slight variation but was equivalent to values reported by Nahrendorf et al. [93]. EF in the MI group at 4 weeks was similar to the value reported by Carr et al. [94], but was higher than those reported by Stuckey et al. [83] and Nahrendorf et al. [27]. The variation in EF in infarcted rats most likely results from variation in infarct size, leading to differences in level of contractility [75].

The analysis time in our study (25 ± 5 minutes) was longer than previously reported values (10 and 8 minutes) using other SASs [79,95]. Nevertheless, these studies conducted cardiac analysis in mouse heart, thus the number of slices covering the whole heart with the same slice thickness was lower.

Time savings for SASs are enormous, compared to manual segmentation. It can range between 20% and 70% depending on the number of cardiac frames segmented manually [78]. In our study, the segmentation time was significantly shorter than reported values using manual segmentation software (53 minutes and 2.5 hours) [78-79], which led to fast and accurate volumetric analysis. The time savings allowed us to perform longitudinal studies and analyze cardiac parameters over time, such as EDV, ESV, EF, SV and CO. Also, it granted us the opportunity to perform regional functional analysis over time.

Similar to a previous study [78], a significant amount of time was spent manually adjusting the contour line defining the epicardial border. Therefore, contrast enhancement between myocardium and surrounding tissues may lead to greater time savings.

9.4 LVM Validation

In our study the results of LVM measured by MRI correlated very well with post-mortem values. In addition, Bland-Altman analysis revealed very low mean difference and low variation (< 15% of mean of true wet LVM) between the two methods. Moreover, these results are in close agreement with previous studies [43,96]. MRI has been considered the gold standard for accurate measurements of LVM in rodents in non-clinical scanners [19,29,97]. However, this study shows that accurate and reliable volumetric and mass measurements can also be performed on data acquired with a 3T clinical scanner.

9.5 Global Functional and Structural Analysis

In the sham group there was no significant variation in SV, CO and LVM at either 2 or 4 weeks (Table 8.2). In the MI group, rats underwent LVR, in terms of functional and structural changes (Table 8.2), after LAD occlusion.

The major functional change was a significant drop in EF due to the large extent of the fibrous tissue (loss of myocardium) causing contractile dysfunction in the heart (Figure 8.5A and Figure 8.8C) [74,98]. The contractile dysfunction also caused significant increase in ESV (Figure 8.6B) at 2 weeks. Furthermore, there was a slight increase in EDV at 2 weeks, which would result in maintenance of SV [75]. The increase in ventricular volumes would likely amplify diastolic and systolic wall stress which can serve as a stimulus for further ventricular dilation [75]. Further significant increase in ESV and EDV was observed at 4 weeks post surgery.

LV hypertrophy was evident in infarcted rats as indicated by severe increase in heart weight and LVM compared with sham rats at both 2 and 4 weeks. This probably occurs due to progressive LV dilation (Table 8.2 and Figure 8.6D) [27].

Increase in LVM was accompanied by LV hypertrophy in posterior and septal regions (Figure 8.8A). This was also observed by Litwin et al. [99] and Rubin et al. [73] and is attributed to increase in myocyte cell volume in order to stabilize contractile function and reduce progressive dilation [100].

9.6 Regional Functional Analysis

In MI group, slight increase in ED WTh was evident at 2 weeks post surgery in all regions of the heart (Figure 8.7A). The increase was probably due to LV hypertrophy in the posterior and septal [100], while in anterior and lateral was probably due to edema [77]. Contrary to ED WTh, modest decrease in ES WTh was observed in the regions of anterior and lateral (Figure 8.7B). Furthermore, %WTh revealed modest reduction in wall thickening in all regions of the heart (Figure 8.7C) probably due to dysfunction in myocardial contractility [75].

At 4 weeks post surgery, collagen scarring was evident in anterior and lateral regions (blue stained region) of the heart (Figure 8.5A). By contrast, rats in the sham group had no scarring (Figure 8.5C and Figure 8.5D), confirming that infarction was induced only by ligation of the

LAD coronary artery in the MI group. In regions with infarction, fibroblasts are transformed into myofibroblasts that are responsible for collagen formation to stabilize distending forces and prevent further deformation [100]. By 3 to 4 weeks, the infarcted region is completely healed by formation of fibrous tissue (collagen scar) (Figure 8.5B) [73,101].

Regional functional analysis at 4 weeks post surgery revealed significant reduction in wall thickness at ED in the anterior region and a modest decrease in the lateral region (Figure 8.8A). This was a result of necrosis of myocytes in infarcted regions [75]. At ES, WTh analysis revealed significant reduction in anterior and lateral regions and modest reduction in the remaining regions of the heart (Figure 8.8B). Furthermore, %WTh revealed reduced wall thickening in all regions that were only significant in lateral and posterior regions (Figure 8.8C). These reductions in ES wall thickness and wall thickening arise due to contractile dysfunction not only in infarcted regions, but also in non-infarcted regions [96,102]. However, anterior and lateral regions showed a greater deficit in function (Figure 8.8A and Figure 8.8B) than other regions because of considerable loss of viable myocardium (Figure 8.5B).

9.7 Limitations

In this study, ECG and respiratory triggering with 3 signal averages were necessary to acquire high quality images. Some images, occasionally, suffered when rats had arrhythmic heartbeats.

Due to long TE and changes in heart rate, some flow and motion artifacts were observed (Figure 9.1); however those artifacts were far away from ED and ES frames, allowing robust and reliable functional and structural assessment of the rat heart. Hardware limitations and dephasing gradient lobes in the FLASH sequence limit the achievable reduction in TE, but implementation of spiral imaging can eradicate flow artifacts [6].

A large flip angle was used to provide high contrast between endocardium and the LV blood. Unfortunately, the epicardium did not benefit from this contrast phenomenon causing ambiguity in delineating the epicardial border. Riegler et al. [78] and Ross et al. [26] reported similar limitations due to the very small contrast between epicardium and surrounding tissue, and susceptibility differences between lung and the heart due to magnetic field inhomogeneities.

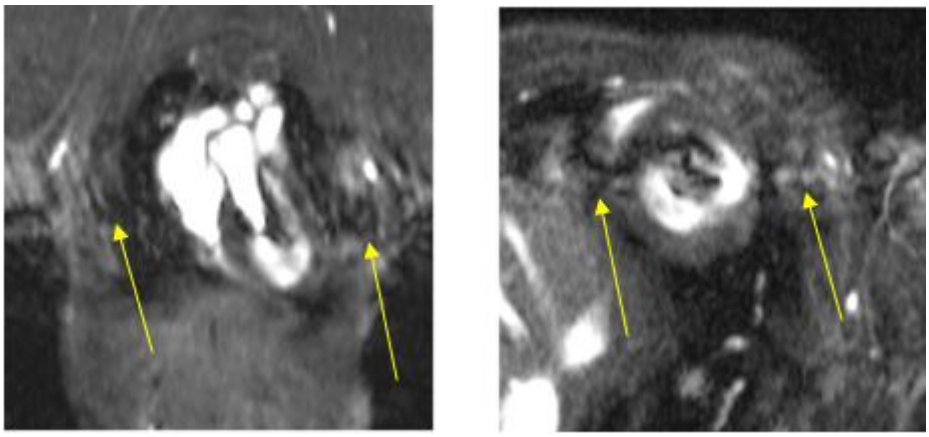

Figure 9.1: Flow artifacts (arrows) due to large TE.

10. Conclusions and Recommendations

In cardiovascular research, small-animal imaging is extensively used for studying cardiac failure at various stages of disease as well as investigating pathophysiological mechanisms and the effects of drug interventions. The current technique implemented at the Cardiovascular Research Unit (CVRU), University of Cape Town, is echocardiography. Although echocardiography is widely used for studying cardiac function and morphology, it relies mostly on geometric assumptions that work well only in normal hearts. The gold standard non-invasive technique for studying cardiac failure over time is MRI, as it offers high temporal and spatial resolution, allowing accurate functional and structural analyses.

Therefore, this study focused on extending clinical MRI, available at CUBIC, to small-animal MRI (MRM). The major challenge in setting up MRM is the attainable SNR. Other challenges include the physical and physiological support needed for the safety and comfort of the animals.

In order to attain higher SNR, a custom built small-animal coil was used. SNR and relative SNR of phantom images acquired using this coil was more than an order of magnitude better than with the standard head coil. This facilitated acquisition of cardiac images with very high spatial resolution.

The cradle was built according to the dimensions of the coil and rat. It accommodates rats and the cables necessary for physiological monitoring. It dissipates heat very well to the animal – and combined with a temperature regulation system – it maintained the temperature of the animal within satisfactory limits (37 ± 0.5 °C). Although the variation was low (± 0.5 °C), future development would be to develop an automatic temperature regulation system, as this could provide an effective way of maintaining the temperature in a narrow range (± 0.1 °C), resulting in great stability in heart rate and reduction in scanning time. The nose cone embedded on the cradle provided excellent means of maintaining anesthesia without any harm to the animal and provided an easy way of controlling the depth of anesthesia.

In order to reduce cardiac and respiratory motion artifacts, we implemented a gating system. The optimized FLASH sequence yielded excellent quality images with superb SNR and CNR, allowing implementation of SASs. The high temporal and spatial resolution made it possible to perform accurate volumetric and WTh analyses, thus revealing important relationships

between LV function and LVR. Several published studies recommend the FLASH sequence for the studies of pathophysiological processes in the rat models of MI.

Future work could include i) addition of gadolinium enhancement to depict the area of infarct in MR images using an Inversion Recovery (IR) sequence, ii) implementation of spiral imaging to eradicate flow artifacts, resulting in better analyses of the heart post MI, and iii) implementation of a bSSFP sequence, as it would improve SNR and CNR of cardiac images. The bSSFP sequence suffers from dark banding artifacts that can be reduced by capturing cardiac images with different synthesizer frequency and utilizing a sum of squares (SOS) method. Due to the brevity of the project timeline, we could not implement this sequence in our study.

We have demonstrated assessment of a rat model of non-reperfused MI using clinical MRI and SASs, called Segment. LVM measured by MRI was validated with post-mortem values, confirming that MRI is well suited to non-invasively and accurately measure LVM in rats. Following the induction of MI, considerable changes in functional (global and regional) and structural parameters were found, which were quantified effectively and accurately with SASs in a short period of time.

This study has shown that clinical 3T MRI with a small-animal coil and optimized GE sequence generated images of rat heart with adequate SNR for successful semi-automatic segmentation to accurately and rapidly evaluate short-term LVR following non-reperfused MI.

The techniques implemented to set up and perform cardiac MRM can be implemented to study different models of heart failure, and because of its non-invasive nature, it allows repeated assessment of cardiac function in the same animal, providing better tracking of pathological changes over time and increases the statistical strength to detect differences. Moreover, the exceptional level of information acquired through this modality may lead to potential treatment strategies.

References

1. Driehuys B, Nouls J, Badea A. Small animal imaging with magnetic resonance microscopy. ILAR journal 2008;49:35 - 53.

2. Nahrendorf M, Badea C, Hedlund LW. High-resolution imaging of murine myocardial infarction with delayed-enhancement cine micro-CT. American Journal of Physiology- Heart and Circulatory Physiology 2007;292(6):H3172-H3178.

3. Johnson GA, Cofer GP, Fubara B, Gewalt SLH, L.W.; Maronpot, R.R. Magnetic resonance histology for morphologic phenotyping. Journal of Magnetic Resonance Imaging 2002;16(4):423-429.

4. Badea CT, Bucholz E, Hedlund LW, Rockman HA, Johnson GA. Imaging methods for morphological and functional phenotyping of the rodent heart. Toxicologic pathology 2006;34(1):111-117.

5. Flint JJ, Choong H. Lee, Brian Hansen f. Magnetic resonance microscopy of mammalian neurons. Neuroimage 2009;46(4):1037-1040.

6. Brau A, Hedlund LW, Johnson GA. Cine magnetic resonance microscopy of the rat heart using cardiorespiratory synchronous projection reconstruction. Journal of Magnetic Resonance Imaging 2004;20(1):31-38.

7. Hashemi RH, William G Bradley J, Lisanti CJ. MRI: The Basics. Philadelphia: Lippincott Williams and Wilkins; 2004.

8. Haacke EM, Brown RW, R TM, R V. Magnetic Resonance Imaging Physical Principles and Sequence Design. New York: Wiley-Liss; 1999.

9. Johnson GA, Cofer GP, Fubara B, Gewalt SLH, L.W.; Maronpot, R.R. Magnetic Resonance Histology for Morphologic Phenotyping. Journal of Magnetic Resonance Imaging 2002;16(4):423 - 429.

10. Redpath TW. Signal-to-noise ratio in MRI. British Journal of Radiology 1998;71:704-707.

11. Maronpot RR, Sills RC, Johnson GA. Applications of magnetic resonance microscopy. Toxicologic Pathology 2004;32:42-48.

12. Gilson WD, Kraitchman DL. Cardiac magnetic resonance imaging in small rodents using clinical 1.5 T and 3.0 T scanners. Methods 2007;43(1):35-45.

13. Doty FD, G; E, Kulkarni J. Radio frequency coil technology for small-animal MRI. NMR in biomedicine 2007;20:304 - 325.

14. Rivera M, Vaquero JJ, Santos A, Ruiz-Cabello J, del Pozo F. MRI visualization of small structures using improved surface coils. Magnetic resonance imaging 1998;16(2):157-166.

15. Gareis D, Wichmann T, Titus Lanz GM, 1 Michael Horn3 and Peter M. Jakob. Mouse MRI using phased-array coils. NMR in Biomedicine 2007;20(3):326-334.

16. Doty FD, G; E, Staab JP. Practical Aspects of Birdcage Coils. Journal of Magnetic Resonance 1999;138:144-154.

17. Schneider JE, Lanz T, Barnes H, et al. Ultra-fast and accurate assessment of cardiac function in rats using accelerated MRI at 9.4 Tesla. Magnetic resonance in medicine 2008;59(3):636-641.

18. Schelbert EB, Hsu LY, Anderson SA, et al. Late Gadolinium-Enhancement Cardiac Magnetic Resonance Identifies Postinfarction Myocardial Fibrosis and the Border Zone at the Near Cellular Level in Ex Vivo Rat HeartClinical Perspective. Circulation: Cardiovascular Imaging 2010;3(6):743.

19. Price AN, Cheung KK, Cleary JO, Campbell AE, Riegler J, Lythgoe MF. Cardiovascular Magnetic Resonance Imaging in Experimental Models. The Open Cardiovascular Medicine Journal 2010;4:278-292.

20. Vallée JP, Ivancevic M, Nguyen D, Morel D, Jaconi M. Current status of cardiac MRI in small animals. Magnetic Resonance Materials in Physics, Biology and Medicine 2004;17(3):149-156.

21. Jones JR, Mata JF, Yang Z, French BA, Oshinski JN. Left ventricular remodeling subsequent to reperfused myocardial infarction: evaluation of a rat model using cardiac magnetic resonance imaging. Journal of Cardiovascular Magnetic Resonance 2002;4(3):317-326.

22. Franco F, Thomas GD, Giroir B, et al. Magnetic resonance imaging and invasive evaluation of development of heart failure in transgenic mice with myocardial expression of tumor necrosis factor-{alpha}. Circulation 1999;99(3):448-454.

23. Delattre B, Braunersreuther V, Hyacinthe JN, Crowe LA, Mach F, Vallée JP. Myocardial infarction quantification with Manganese Enhanced MRI (MEMRI) in mice using a 3T clinical scanner. NMR in Biomedicine 2010;23(5):503-513.

24. Foster-Gareau P, Heyn C, Alejski A, Rutt BK. Imaging single mammalian cells with a 1.5 T clinical MRI scanner. Magnetic resonance in medicine 2003;49(5):968-971.

25. Hubrecht R, Kirkwood J. The UFAW Handbook on the Care and Management of Laboratory and Other Research Animals. Hubrecht R, Kirkwood J, editors: Wiley-Blackwell; 2010.

26. Ross AJ, Yang Z, Berr SS, et al. Serial MRI evaluation of cardiac structure and function in mice after reperfused myocardial infarction. Magnetic resonance in medicine 2002;47(6):1158-1168.

27. Nahrendorf M, Wiesmann F, Hiller KH, et al. Serial cine magnetic resonance imaging of left ventricular remodeling after myocardial infarction in rats. Journal of Magnetic Resonance Imaging 2001;14(5):547-555.

28. Nahrendorf M, Hiller KH, Hu K, Ertl G, Haase A, Bauer W. Cardiac magnetic resonance imaging in small animal models of human heart failure. Medical Image Analysis 2003;7(3):369-375.

29. Protti A, Sirker A, Shah AM, Botnar R. Late gadolinium enhancement of acute myocardial infarction in mice at 7T: Cine FLASH versus inversion recovery. Journal of Magnetic Resonance Imaging 2010;32(4):878-886.

30. Cassidy PJ, Schneider JE, Grieve SM, Lygate C, Neubauer S, Clarke K. Assessment of motion gating strategies for mouse magnetic resonance at high magnetic fields. Journal of Magnetic Resonance Imaging 2004;19(2):229-237.

31. Scheffler K, Lehnhardt S. Principles and applications of balanced SSFP techniques. European radiology 2003;13(11):2409-2418.

32. Nahrendorf M, Streif JU, Hiller KHH KN, P.; Ritter, O.; Sosnovik, D.; Bauer, L.; Neubauer, S.; Jakob, P.M. . Multimodal functional cardiac MRI in creatine kinase-deficient mice reveals subtle abnormalities in myocardial perfusion and mechanics. American Journal of Physiology-Heart and Circulatory Physiology 2006;290(6):H2516 - H2521.

33. Yang Z, Berr SS, Gilson WD TM, B.A. . Simultaneous evaluation of infarct size and cardiac function in intact mice by contrast-enhanced cardiac magnetic resonance imaging reveals contractile dysfunction in noninfarcted regions early after myocardial infarction. Circulation 2004;109(9):1161 - 1167.

34. Ruff J, Wiesmann F, Hiller KH VS, M.; Bauer, W.R.; Rommel, E.; Neubauer, S.; Haase, . 1998;40(1):43 - 8. Magnetic resonance microimaging for noninvasive quantification of myocardial function and mass in the mouse. Magnetic Resonance in Medicine 1998;40(1):43-48.

35. Rehwald W G, Reeder SB, McVeigh ERJ RM. Techniques for high-speed cardiac magnetic resonance imaging in rats and rabbits. Magnetic Resonance in Medicine 1997;37(1):124-130.

36. Bernstein MA, King KE, Zhou XJ, Fong W. Handbook of MRI pulse sequences. Medical Physics 2005;32:1452.

37. Hargreaves B. Fast Gradient Echo Sequences Including Balanced SSFP.

38. Bohl S, Lygate CA, Barnes H, et al. Advanced methods for quantification of infarct size in mice using three-dimensional high-field late gadolinium enhancement MRI. American Journal of Physiology-Heart and Circulatory Physiology 2009;296(4):H1200-H1208.

39. Thomas D, Dumont C, Pickup S, et al. T1-weighted cine FLASH is superior to IR imaging of post-infarction myocardial viability at 4.7 T. Journal of Cardiovascular Magnetic Resonance 2006;8(2):345-352.

40. Finn JP, Nael K, Deshpande V, Ratib O, Laub G. Cardiac MR Imaging: State of the Technology1. Radiology 2006;241(2):338-354.

41. Heijman E, De Graaf W, Niessen P, et al. Comparison between prospective and retrospective triggering for mouse cardiac MRI. NMR in Biomedicine 2007;20(4):439-447.

42. Atkinson DJ, Edelman R. Cineangiography of the heart in a single breath hold with a segmented turboFLASH sequence. Radiology 1991;178(2):357-360.

43. Ruff J, Wiesmann F, Hiller KH, et al. Magnetic resonance microimaging for noninvasive quantification of myocardial function and mass in the mouse. Magnetic resonance in medicine 1998;40(1):43-48.

44. Colby LA, Morenko BJ. Clinical considerations in rodent bioimaging. Comparative medicine 2004;54(6):623-630.

45. McRobbie DW. MRI from picture to proton: Cambridge Univ Pr; 2003.

46. Benveniste H, Blackband S. MR microscopy and high resolution small animal MRI: applications in neuroscience research. Progress in Neurobiology 2002;67:393-420.

47. Koolhaas JM. The Laboratory Rat. The UFAW Handbook on the Care and Management of Laboratory and Other Research Animals: Wiley-Blackwell, 2010; 311-326.

48. Heijman E, Strijkers GJ, Habets J. Magnetic resonance imaging of regional cardiac function in the mouse. Magnetic Resonance Materials in Physics, Biology and Medicine 2004;17:170-178.

49. Thorsen F, Ersland L, Nordli H. Imaging of experimental rat gliomas using a clinical MR scanner. Journal of neuro-oncology 2003;63:225-231.

50. Bucholz E, Ghaghada K, Qi Y. Cardiovascular phenotyping of the mouse heart using a 4D radial acquisition and liposomal Gd-DTPA-BMA. Magnetic Resonance in Medicine 2010;63:979-987.

51. Xu S, Gade; TPF, Matei; C. In Vivo Multiple-Mouse Imaging at 1.5 T. Magnetic Resonance in Medicine 2003;49: 551 - 557.

52. Langer S, Paulus N, Heiss C, et al. Cardiovascular remodeling after AVF surgery in rats assessed by a clinical MRI scanner. Magnetic resonance imaging 2011;29(1):57-63.

53. Numano T, Marushima A, Hyodo K, Homma K, Suzuki K, Matsumura A. Three-dimensional diffusion weighted imaging of the acute cerebral ischemia rat using 3D MP-RAGE MRI. 2010. IEEE. p 3179-3182.

54. Roth DM, Swaney JS, Dalton ND, Gilpin EA, Ross J. Impact of anesthesia on cardiac function during echocardiography in mice. American Journal of Physiology-Heart and Circulatory Physiology 2002;282(6):H2134.

55. Kober F, Iltis I, Cozzone P, Bernard M. Cine-MRI assessment of cardiac function in mice anesthetized with ketamine/xylazine and isoflurane. Magnetic Resonance Materials in Physics, Biology and Medicine 2004;17(3):157-161.

56. Balaban RS, Hampshire VA. Challenges in small animal noninvasive imaging. ILAR journal 2001;42(3):248-262.

57. Rengle A, Baboi L, Saint-Jalmes H. Optical cardiac and respiratory device for synchronized MRI on small animal.; 2007; Lyon, France. p 2046-2049.

58. Colby LA, Morenko BJ. Clinical considerations in rodent bioimaging. Comparative medicine 2004;54(6):623 - 630.

59. Rehwald WG, Reeder SB, McVeigh ER, Judd RM. Techniques for high-speed cardiac magnetic resonance imaging in rats and rabbits. Magnetic resonance in medicine 1997;37(1):124-130.

60. Hedlund LW, Johnson GA. Mechanical ventilation for imaging the small animal lung. Invest Radiol 2002;21:18-23.

61. Costa D, Lehmann J, Harold W, Drew R. Transoral tracheal intubation of rodents using a fiberoptic laryngoscope. Laboratory animal science 1986;36(3):256.

62. Morton D, Jennings M, Buckwell A, et al. Refining procedures for the administration of substances. Report of the BVAAWF/FRAME/RSPCA/UFAW Joint Working Group on Refinement. British Veterinary Association Animal Welfare Foundation/Fund for the Replacement of Animals in Medical Experiments/Royal Society for the Prevention of Cruelty to Animals/Universities Federation for Animal Welfare. Laboratory animals 2001;35(1):1.

63. Nahrendorf M, Streif JU, Hiller KH, et al. Multimodal functional cardiac MRI in creatine kinase-deficient mice reveals subtle abnormalities in myocardial perfusion and mechanics. American Journal of Physiology-Heart and Circulatory Physiology 2006;290(6):H2516-H2521.

64. Ivancevic MK, Daire J-L, Vallée JP. High-resolution complementary spatial modulation of magnetization (CSPAMM) rat heart tagging on a 1.5 Tesla Clinical Magnetic Resonance System: A preliminary feasibility study. Investigative Radiology 2007;42:204-210.

65. Epstein FH, Yang Z, Gilson WD, Berr SS, Kramer CM, French BA. MR tagging early after myocardial infarction in mice demonstrates contractile dysfunction in adjacent and remote regions. Magnetic resonance in medicine 2002;48(2):399-403.

66. Ojha N, Roy S, Radtke J, et al. Characterization of the structural and functional changes in the myocardium following focal ischemia-reperfusion injury. American Journal of Physiology-Heart and Circulatory Physiology 2008;294(6):H2435-H2443.

67. Bushong SC. Magnetic resonance imaging: physical and biological principles: St. Louis: Mosby; 1996.

68. Muders F, Elsner D. Animal models of chronic heart failure. Pharmacological Research 2000;41(6):605-612.

69. Balakumar P, Singh AP, Singh M. Rodent models of heart failure. Journal of pharmacological and toxicological methods 2007;56(1):1-10.

70. Patten RD, Aronovitz MJ, Deras-Mejia L, et al. Ventricular remodeling in a mouse model of myocardial infarction. American Journal of Physiology-Heart and Circulatory Physiology 1998;274(5):H1812.

71. Medvedev OS, Gorodetskaya EA. Systemic and regional hemodynamic effects of perindopril in experimental heart failure. American Heart Journal 1993;126(3):764-769.

72. Patten RD, Hall-Porter MR. Small Animal Models of Heart Failure. Circulation: Heart Failure 2009;2(2):138-144.

73. Rubin SA, Fishbein MC, Swan H. Compensatory hypertrophy in the heart after myocardial infarction in the rat. Journal of the American College of Cardiology 1983;1(6):1435-1441.

74. Pfeffer MA, Pfeffer JM, Fishbein M, et al. Myocardial infarct size and ventricular function in rats. Circulation Research 1979;44(4):503-512.

75. Pfeffer MA, Braunwald E. Ventricular remodeling after myocardial infarction. Experimental observations and clinical implications. Circulation 1990;81(4):1161-1172.

76. Pfeffer M, Pfeffer J, Steinberg C, Finn P. Survival after an experimental myocardial infarction: beneficial effects of long-term therapy with captopril. Circulation 1985;72(2):406-412.

77. Holmes JW, Borg TK, Covell JW. Structure and mechanics of healing myocardial infarcts. Annu Rev Biomed Eng 2005;7:223-253.

78. Riegler J, Cheung KK, Man YF, Cleary JO, Price AN, Lythgoe MF. Comparison of segmentation methods for MRI measurement of cardiac function in rats. Journal of Magnetic Resonance Imaging 2010;32(4):869-877.

79. Heijman E, Aben JP, Penners C, et al. Evaluation of manual and automatic segmentation of the mouse heart from CINE MR images. Journal of Magnetic Resonance Imaging 2008;27(1):86-93.

80. Heiberg E, Wigstrom L, Carlsson M, Bolger A, Karlsson M. Time resolved three-dimensional automated segmentation of the left ventricle. 2005. IEEE. p 599-602.

81. Schalla S, Wendland MF, Higgins CB, Ebert W, Saeed M. Accentuation of high susceptibility of hypertrophied myocardium to ischemia: Complementary assessment of Gadophrin- enhancement and left ventricular function with MRI. Magnetic resonance in medicine 2004;51(3):552-558.

82. Shah DJ, Judd RM, Kim RJ. Technology insight: MRI of the myocardium. Nature Clinical Practice Cardiovascular Medicine 2005;2(11):597-605.

83. Stuckey DJ, Carr CA, Tyler DJ, Clarke K. Cine MRI versus two dimensional echocardiography to measure in vivo left ventricular function in rat heart. NMR in Biomedicine 2008;21(7):765-772.

84. van Geuns RJM, Baks T, Gronenschild EHBM, et al. Automatic Quantitative Left Ventricular Analysis of Cine MR Images by Using Three-dimensional Information for Contour Detection1. Radiology 2006;240(1):215-221.

85. Barkhausen J, Ruehm SG, Goyen M, Buck T, Laub G, Debatin JF. MR Evaluation of Ventricular Function: True Fast Imaging with Steady-State Precession versus Fast Low-Angle Shot Cine MR Imaging: Feasibility Study1. Radiology 2001;219(1):264-269.

86. Young AA, Cowan BR, Thrupp SF, Hedley WJ, Dell'Italia LJ. Left Ventricular Mass and Volume: Fast Calculation with Guide-Point Modeling on MR Images1. Radiology 2000;216(2):597-602.

87. Sievers B, Kirchberg S, Bakan A, Franken U, Trappe HJ. Impact of papillary muscles in ventricular volume and ejection fraction assessment by cardiovascular magnetic resonance. Journal of Cardiovascular Magnetic Resonance 2004;6(1):9-16.

88. Dobner S, Bezuidenhout D, Govender P, Zilla P, Davies N. A synthetic non-degradable polyethylene glycol hydrogel retards adverse post-infarct left ventricular remodeling. Journal of cardiac failure 2009;15(7):629-636.

89. Barbier EC, Johansson L, Lind L, Ahlström H, Bjerner T. The exactness of left ventricular segmentation in cine magnetic resonance imaging and its impact on systolic function values. Acta Radiologica 2007;48(3):285-291.

90. Takagawa J, Zhang Y, Wong ML, et al. Myocardial infarct size measurement in the mouse chronic infarction model: comparison of area-and length-based approaches. Journal of Applied Physiology 2007;102(6):2104-2111.

91. Martin Bland J, Altman DG. Statistical methods for assessing agreement between two methods of clinical measurement. The Lancet 1986;327(8476):307-310.

92. Thomas D, Ferrari V, Janik M, et al. Quantitative assessment of regional myocardial function in a rat model of myocardial infarction using tagged MRI. Magnetic Resonance Materials in Physics, Biology and Medicine 2004;17(3):179-187.

93. Nahrendorf M, Hiller KH, Greiser A, et al. Chronic coronary artery stenosis induces impaired function of remote myocardium: MRI and spectroscopy study in rat. American Journal of Physiology-Heart and Circulatory Physiology 2003;285(6):H2712-H2721.

94. Carr CA, Stuckey DJ, Tatton L, et al. Bone marrow-derived stromal cells home to and remain in the infarcted rat heart but fail to improve function: an in vivo cine-MRI study. American Journal of Physiology-Heart and Circulatory Physiology 2008;295(2):H533-H542.

95. Young AA, Barnes H, Davison D, Neubauer S, Schneider JE. Fast left ventricular mass and volume assessment in mice with three- dimensional guide- point modeling. Journal of Magnetic Resonance Imaging 2009;30(3):514-520.

96. Yang Z, Berr SS, Gilson WD, Toufektsian MC, French BA. Simultaneous evaluation of infarct size and cardiac function in intact mice by contrast-enhanced cardiac magnetic resonance imaging reveals contractile dysfunction in noninfarcted regions early after myocardial infarction. Circulation 2004;109(9):1161-1167.

97. Slawson SE, Roman BB, Williams DS, Koretsky AP. Cardiac MRI of the normal and hypertrophied mouse heart. Magnetic resonance in medicine 1998;39(6):980-987.

98. Hori M, Inoue M, Fukui S, et al. Correlation of ejection fraction and infarct size estimated from the total CK released in patients with acute myocardial infarction. British Heart Journal 1979;41(4):433-440.

99. Litwin SE, Katz SE, Morgan JP, Douglas PS. Serial echocardiographic assessment of left ventricular geometry and function after large myocardial infarction in the rat. Circulation 1994;89(1):345-354.

100. Sutton MG, Sharpe N. Left ventricular remodeling after myocardial infarction: pathophysiology and therapy. Circulation 2000;101(25):2981-2988.

101. Cleutjens JPM, Kandala JC, Guarda E, Guntaka RV, Weber KT. Regulation of collagen degradation in the rat myocardium after infarction. Journal of molecular and cellular cardiology 1995;27(6):1281-1292.

102. French BA, Kramer CM. Mechanisms of postinfarct left ventricular remodeling. Drug Discovery Today: Disease Mechanisms 2007;4(3):185-196.